

Emergent lattices with geometrical frustration in doped extended Hubbard models

Ryui Kaneko,¹ Luca F. Tocchio,² Roser Valentí,¹ and Claudius Gros¹

¹*Institute for Theoretical Physics, University of Frankfurt,
Max-von-Laue-Straße 1, D-60438 Frankfurt a.M., Germany*

²*Democritos National Simulation Center, Istituto Officina dei Materiali del CNR,
and SISSA-International School for Advanced Studies, Via Bonomea 265, I-34136 Trieste, Italy*
(Dated: September 12, 2018)

Spontaneous charge ordering occurring in correlated systems may be considered as a possible route to generate effective lattice structures with unconventional couplings. For this purpose we investigate the phase diagram of doped extended Hubbard models on two lattices: (i) the honeycomb lattice with on-site U and nearest-neighbor V Coulomb interactions at $3/4$ filling ($n = 3/2$) and (ii) the triangular lattice with on-site U , nearest-neighbor V , and next-nearest-neighbor V' Coulomb interactions at $3/8$ filling ($n = 3/4$). We consider various approaches including mean-field approximations, perturbation theory, and variational Monte Carlo. For the honeycomb case (i), charge order induces an effective triangular lattice at large values of U/t and V/t , where t is the nearest-neighbor hopping integral. The nearest-neighbor spin exchange interactions on this effective triangular lattice are antiferromagnetic in most of the phase diagram, while they become ferromagnetic when U is much larger than V . At $U/t \sim (V/t)^3$, ferromagnetic and antiferromagnetic exchange interactions nearly cancel out, leading to a system with four-spin ring-exchange interactions. On the other hand, for the triangular case (ii) at large U and finite V' , we find no charge order for small V , an effective kagome lattice for intermediate V , and one-dimensional charge order for large V . These results indicate that Coulomb interactions induce [case (i)] or enhance [case(ii)] emergent geometrical frustration of the spin degrees of freedom in the system, by forming charge order.

PACS numbers: 71.10.Fd, 71.27.+a, 75.25.Dk

I. INTRODUCTION

Correlated systems with competing on-site and inter-site Coulomb interactions¹ and fillings away from one electron per site ($n = 1$, half filling) are presently a subject of intensive investigation due to the appearance of complex phases such as unconventional charge and magnetic orders. These systems become even more challenging when novel lattice structures emerge out of the original lattice in the region of strong correlations². This phenomenon is often found in geometrically frustrated systems, such as triangular and kagome lattices.

On the triangular lattice, for instance, large on-site U and nearest-neighbor V Coulomb interactions generate effective honeycomb and enlarged triangular lattices at $1/3$ filling ($n = 2/3$) by inducing charge disproportionation^{3–5}. When $V \gtrsim U/3$ the system tends to create a honeycomb lattice of empty sites and an enlarged triangular lattice of doubly occupied sites, while at smaller ratios of V/U the system evolves into a honeycomb lattice of singly occupied sites with long-range antiferromagnetic order. A similar charge ordered state with noncollinear magnetic order has also been proposed in the Kondo lattice system⁶. While these states are insulating, such exotic charge and magnetic orders become metallic away from the commensurate filling⁴. Furthermore, at quarter filling ($n = 1/2$), metallic states, named pinball liquids, have been also recently proposed^{7–10}. They are characterized by a three-sublattice structure, in which the carriers of one sublattice are essentially localized (pins), with the remaining charges (balls) building an itinerant liquid

on the interstitials. Recently, other mechanisms than direct charge disproportionation have been also proposed to generate new lattice structures such as the emergence of a kagome lattice via spontaneous ferrimagnetic order coexisting with a $\sqrt{3} \times \sqrt{3}$ charge order pattern in a triangular Kondo lattice¹¹.

Similarly, on the kagome lattice, large values of U and V have been discussed to induce nearly isolated six-site rings and an enlarged kagome lattice at $1/3$ filling ($n = 2/3$)^{12–14}. Specifically, when $U, V > 0$ and $t = 0$, each corner-sharing triangle possesses charge order characterized by two singly occupied sites and an empty site. The empty site randomly sits on one of the three vertices of a triangle, which gives macroscopic charge degeneracy. Nonzero hopping t lifts the charge degeneracy and appears to stabilize a $\sqrt{3} \times \sqrt{3}$ charge pattern, whose unit cell contains nine sites^{12–14}. Recently, by mapping the system into a hard-core boson Hamiltonian, a topological liquid was also proposed¹⁵.

Reported realizations of such emergent lattices are for instance the generation of a honeycomb structure through charge disproportion in the metallic magnet AgNiO_2 ^{16,17} or the appearance of effective spin-1/2 chains in the heavy-fermion spinel LiV_2O_4 ^{18,19}.

Actually, even when the lattice structures themselves are not geometrically frustrated, such a formation of new lattices is possible due to strong electron correlations. For example, in the cubic lattice, a staggered (π, π, π) charge order generates doubled face-centered-cubic lattices²⁰. Moreover, effective spin and charge interactions in such systems may acquire additional geo-

metrical frustrations. Indeed, unconventional noncoplanar magnetic orders have been proposed in the periodic Anderson model on the cubic lattice at $n = 3/2$ filling²⁰.

One of the most discussed bipartite lattices in two-dimensional systems is the honeycomb lattice. While correlation effects on the honeycomb lattice have been intensively discussed in the past, many studies focused mostly at half filling^{21–28}. Castro *et al.*²⁹ and Grushin *et al.*³⁰ studied extensively the phase diagram in honeycomb systems for arbitrary filling; however, they considered only the spinless Hubbard model.

In this work, we investigate the possible emergence of correlation-induced new lattice structures both in a bipartite and in a geometrically frustrated lattice at fillings that, to our knowledge, have not been investigated before. In particular, we perform an extensive analysis of the spinful extended Hubbard model on honeycomb and triangular lattices away from half filling, and focus on the interplay between on-site U and intersite nearest- and next-nearest Coulomb interactions V and V' , respectively. By using the Hartree-Fock approximation, as well as perturbation theory and the variational Monte Carlo method, we find that a triangular structure emerges from charge order on the honeycomb lattice for large values of U and V at $3/4$ filling ($n = 3/2$, three electrons per two sites on average). Charge-poor sites possess spin degrees of freedom, and their spin correlations are found to be antiferromagnetic in most of the phase diagram, while they become ferromagnetic when U is much larger than V .

On the other hand, for the triangular lattice with U , V , and V' interactions at $3/8$ filling ($n = 3/4$, three electrons per four sites on average), considering large values of U and a finite V' (we set $V' = V/5$), we find that the system shows rich charge orders: a kagome structure emerges for intermediate values of V , while a one-dimensional structure is stabilized for large values of V . Both examples show an enhancement of geometrical frustration, from the honeycomb to the triangular lattice in the former case, and from the triangular to the kagome in the latter one.

The paper is organized as follows. In Sec. II, we present the extended Hubbard model on the honeycomb lattice and show the possible phases of the model as a function of U and V obtained with the Hartree-Fock approximation and with variational Monte Carlo. We also discuss how U and V determine magnetic patterns of the emergent charge ordered states by means of perturbation theory. In Sec. III, we present variational Monte Carlo results for the extended Hubbard model on the triangular lattice and discuss possible phases of the model as a function of V for large U and $V' = V/5$. Finally, in Sec. IV, we draw our conclusions.

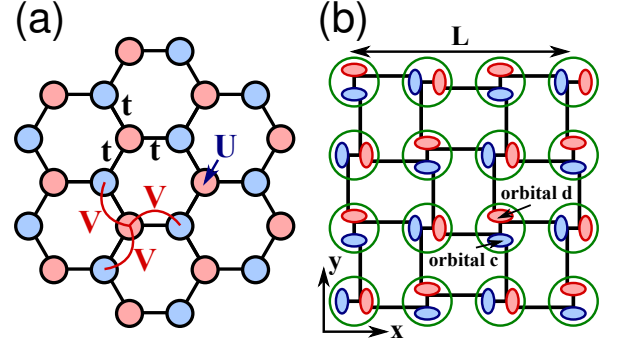


FIG. 1: (Color online) The extended Hubbard model with hopping t , on-site Coulomb interaction U , and nearest-neighbor Coulomb interaction V , Eq. (1) and Eq. (2), on (a) the honeycomb lattice and (b) its equivalent two-band representation, Eq. (2). Blue and red circles denote orbitals c and d , respectively.

II. EMERGENT TRIANGULAR STRUCTURE ON A HONEYCOMB SYSTEM

A. Extended Hubbard model on a honeycomb lattice

We consider an extended Hubbard model on the isotropic honeycomb lattice [see Fig. 1(a)] where the Hamiltonian is given as

$$H = -t \sum_{\langle i,j \rangle, \sigma} c_{i,\sigma}^\dagger c_{j,\sigma} + \text{h.c.} + U \sum_i n_{i,\uparrow} n_{i,\downarrow} + V \sum_{\langle i,j \rangle} n_i n_j; \quad (1)$$

t denotes the hopping parameter, and U and V are the on-site and nearest-neighbor Coulomb interaction, respectively. Hereafter, we investigate repulsive Coulomb interactions ($U, V \geq 0$), and focus on $3/4$ filling ($n = 3/2$). We note that on the honeycomb lattice $3/4$ and $1/4$ fillings are equivalent via the particle-hole transformation.

This model, being defined on a lattice with two sites per unit cell, can be also regarded as a two-band (two-orbital) Hubbard model whose hoppings connect only different orbitals [see Fig. 1(b)],

$$H = -t \sum_{i,\sigma} \left(d_{i,\sigma}^\dagger c_{i,\sigma} + d_{i,\sigma}^\dagger c_{i+e_x,\sigma} + d_{i,\sigma}^\dagger c_{i+e_y,\sigma} + \text{h.c.} \right) + U \sum_i (n_{i,\uparrow}^c n_{i,\downarrow}^c + n_{i,\uparrow}^d n_{i,\downarrow}^d) + V \sum_i \left(n_i^d n_i^c + n_i^d n_{i+e_x}^c + n_i^d n_{i+e_y}^c \right), \quad (2)$$

Both representations of the Hamiltonian are equivalent and we will make use of the latter representation for computational purposes.

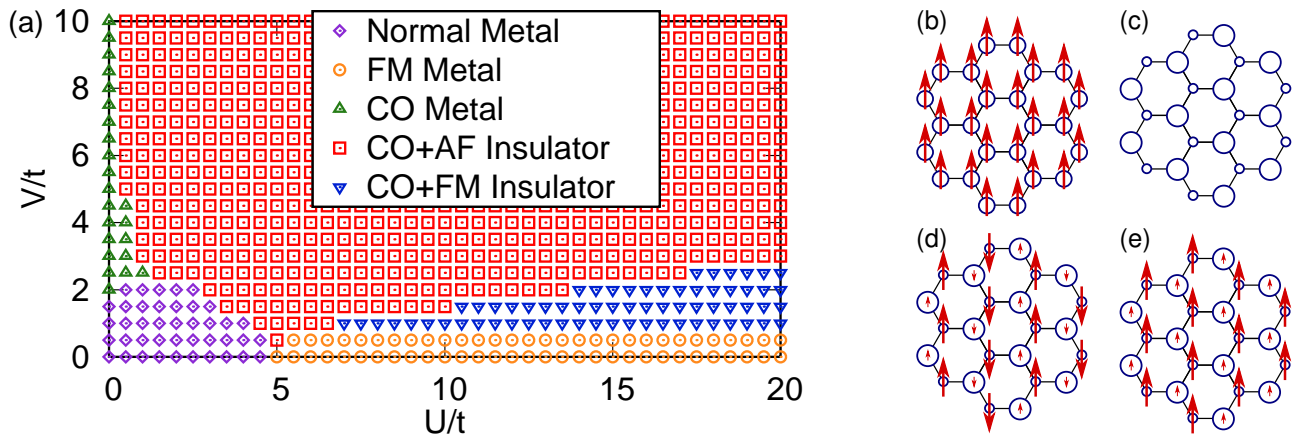


FIG. 2: (Color online) (a) Hartree-Fock phase diagram of the Hubbard model at $n = 3/2$, see Eq. (1), on the honeycomb lattice. (b) Illustration of the ferromagnetic metallic state (FM metal), with one up-spin and half a down-spin (on average) per site. (c) Charge ordered metallic state (CO metal), with alternating doubly and singly occupied site (large/small circles). (d) Charge ordered antiferromagnetic insulating state (CO+AF insulator). (e) Charge ordered ferromagnetic insulating state (CO+FM insulator).

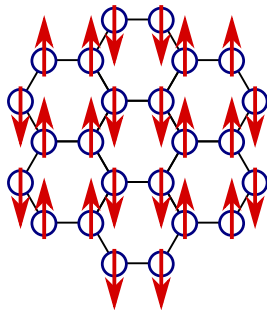


FIG. 3: (Color online) Metastable state found at $V = 0$. Antiferromagnetic (up-up-down-down) insulator without charge order.

B. Mean-field phase diagram

In order to investigate the interplay between charge and magnetic order, we start with a mean-field analysis of the above presented Hamiltonian. Figure 2 (a) shows the U - V phase diagram of the honeycomb model of Eq. (2) at $3/4$ filling obtained with the restricted Hartree-Fock method (as explained in Appendix A.1). For simplicity, we have restricted ourselves to coplanar magnetic order patterns.

In the absence of nearest-neighbor Coulomb interaction V (along $V = 0$) we find four ground-state candidates: normal metal, ferromagnetic metal [Fig. 2(b)], and antiferromagnetic insulator with and without charge order [see Fig. 2(d) and Fig. 3]. As shown in Fig. 4(a), the energies of antiferromagnetic and charge ordered states are always higher than those of normal and ferromagnetic metal states. A continuous phase transition from normal to ferromagnetic metal occurs at $U/t \sim 5$, as shown in Fig. 4(b). This ferromagnetic metal [Fig. 2 (b)] is consistent with the result obtained by Hanisch *et al.*³¹. When

$U/t \gtrsim 6$, spins are fully polarized. In the ferromagnetic state at $3/4$ filling, the up-spin lower band is fully occupied while the down-spin upper band is half filled and the density of states (DOS) is zero at the Fermi energy indicating a semimetallic behavior. Figure 4(c) shows the DOS as a function of U .

On the other hand, in the absence of on-site Coulomb interaction U (along $U = 0$) and for finite V , within the 2×2 sublattice structure, we obtain a staggered charge order state, where c -orbital sites are charge-rich ($n_c = n_{c\uparrow} + n_{c\downarrow} > 3/2$) while d -orbital sites are charge-poor ($n_d = n_{d\uparrow} + n_{d\downarrow} < 3/2$), as shown in Fig. 2(c). In the absence of on-site Coulomb interaction ($U = 0$), this charge ordered state does not have any magnetic order. As shown in Fig. 5, we find a phase transition from the nonmagnetic metal to the charge ordered metal at $V/t \sim 2$ which is stabilized by splitting the upper and lower bands. This state is metallic since the upper band is always half filled for $n = 3/2$.

We consider now the case of large U and V values, where charge order is expected to generate complex magnetic orders. As shown in Fig. 2 (a), when both U and V are large, we find a charge ordered antiferromagnetic insulator. It has a rich-poor-rich-poor type charge pattern, and the charge-poor sites form an emergent triangular structure. Magnetic order is found to be collinear and shows stripe order [Fig. 2 (d)]. On the other hand, when U is much larger than V , a charge ordered ferromagnetic insulating phase [Fig. 2 (e)] appears. It also has triangular-like charge order, and charge-poor sites show dominant ferromagnetic order.

In order to investigate the possible antiferromagnetic patterns on the emergent triangular structure, we consider the collinear and the commensurate spiral state with 120° order of Fig. 6 along the $U = V$ line of the phase diagram. We note that, in general, magnetic states may show incommensurate coplanar spiral order or non-

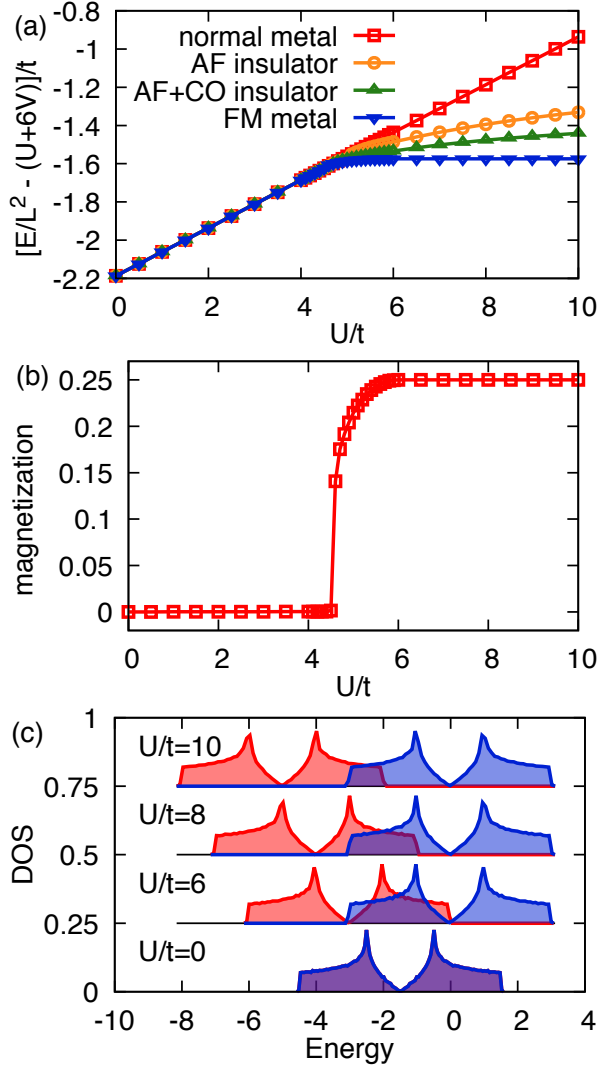


FIG. 4: (Color online) Results for the honeycomb lattice at 3/4 filling for $V = 0$ obtained by the Hartree-Fock method. (a) Energy of each state as a function of U/t . (b) Magnetization of the metallic ground state (normal and FM). (c) Density of states for the ground-state FM metal at each value of U/t . The Fermi level is set to 0. When the up-spin band is completely below the Fermi level, the state becomes semimetallic.

coplanar order in doped Hubbard models³². However, here we restrict ourselves to the coplanar case. As shown in Fig. 7, the stripe antiferromagnetic charge ordered state is found to have a lower energy than the 120° Néel ordered state, although the energy difference becomes extremely small as U and V increase.

The stability of the collinear phase should be induced by second-order processes where a doubly occupied site is formed in the charge-poor sublattice, after the hopping of one electron from the charge-rich sublattice. Indeed, the hopping of one electron from a doubly occupied site to a singly occupied neighboring one is favored when collinearity holds, even for large values of U and V . Since

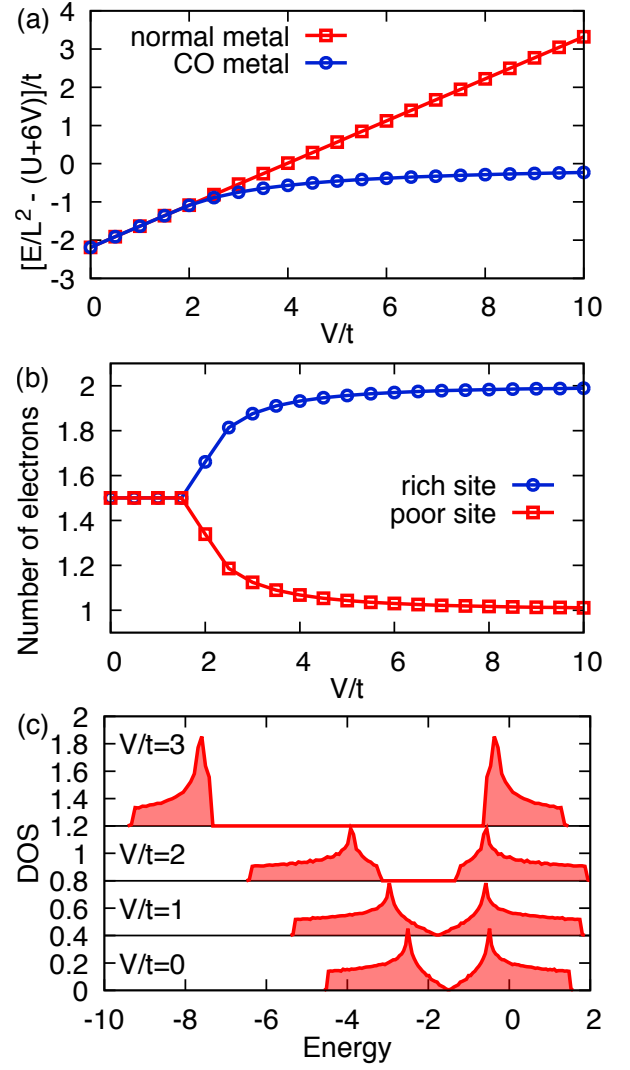


FIG. 5: (Color online) Results for the honeycomb lattice at 3/4 filling for $U = 0$ obtained by the Hartree-Fock method. (a) Energy of metallic states as a function of V/t . (b) The number of electrons per each sublattice for the metallic ground states (with and without charge order). (c) Density of states for the ground-state metallic states. The Fermi level is set to 0.

the intermediate state costs an energy $2V$, see for instance the first part of the process in Fig. A.1, the energy of the second-order process scales as t^2/V , as confirmed by the Hartree-Fock calculations for both stripe and 120° Néel antiferromagnetic charge ordered states in the insulating phase. Moreover, as discussed in Appendix A.4, effective next-neighbor exchange couplings on the emergent triangular lattice are generated for moderately large values of U and V , favoring collinear orderings^{33,34}. All these contributions may then break down the 120° Néel spin state, and induce the observed collinear pattern.

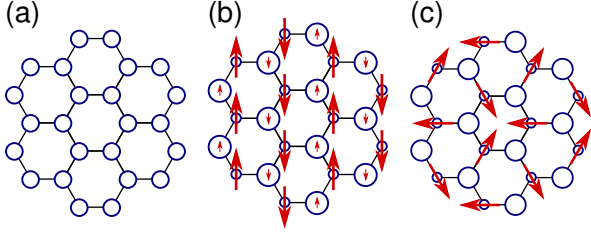


FIG. 6: (Color online) States found for $U = V$. (a) Normal metal without charge and magnetic order. (b) Charge ordered stripe antiferromagnetic insulator. (c) Charge ordered 120° antiferromagnetic insulator. The energy of the stripe antiferromagnetic state is found to be the lowest one.

C. Spin correlation in charge ordered states

In the previous section, we showed that when correlations generate staggered charge order patterns on the honeycomb lattice, charge-rich and charge-poor sites form triangular lattices, respectively. At $3/4$ filling, charge-rich sites contain two electrons on average, while charge-poor sites contain one electron on average with spin degrees of freedom. In order to investigate how magnetic order appears in this limit, we apply perturbation theory to obtain an effective spin Hamiltonian.

At the lowest order, the effective low-energy spin Hamiltonian on the triangular lattice (see Fig. 8) contains a spin exchange interaction and a three-particle permutation term, namely,

$$H_{\text{spin}} = J_1 \sum_{\langle i,j \rangle_1} \mathbf{S}_i \cdot \mathbf{S}_j \quad (3)$$

and

$$H_{\text{perm}} = K_3 \sum_{\triangle} (P_3 + P_3^{-1}). \quad (4)$$

(Further details are given in Appendix A.4.) Here, the sum is taken over all nearest-neighbor sites denoted by $\langle i,j \rangle_1$ for H_{spin} , while it is taken over all triangles, which connect charge-poor sites, for H_{perm} , as illustrated in Fig. 8. The symbol P_n denotes a cyclic permutation operator.

By considering virtual hopping processes, as shown in Fig. A.1, the exchange interaction J_1 can be evaluated as a function of t , U , and V , namely, $J_1 = c_1 t^4 / (V^2 U)$ with a positive constant $c_1 = 1$. This results in antiferromagnetic spin correlations.

Similarly, the coefficient K_3 in the permutation terms can be evaluated by considering six cyclic processes for right-pointing triangles that lie inside the hexagons (K_3^{\triangleright}) and for left-pointing triangles that connect three hexagons (K_3^{\triangleleft}). In Appendix A.4 we show in Fig. A.3 one of the virtual processes generating K_3^{\triangleright} , which does not require the formation of intermediate double-occupied sites. This coefficient survives even for $U = \infty$, namely, $K_3^{\triangleright} = -d_3 t^6 / V^5$ with a positive constant d_3 . When

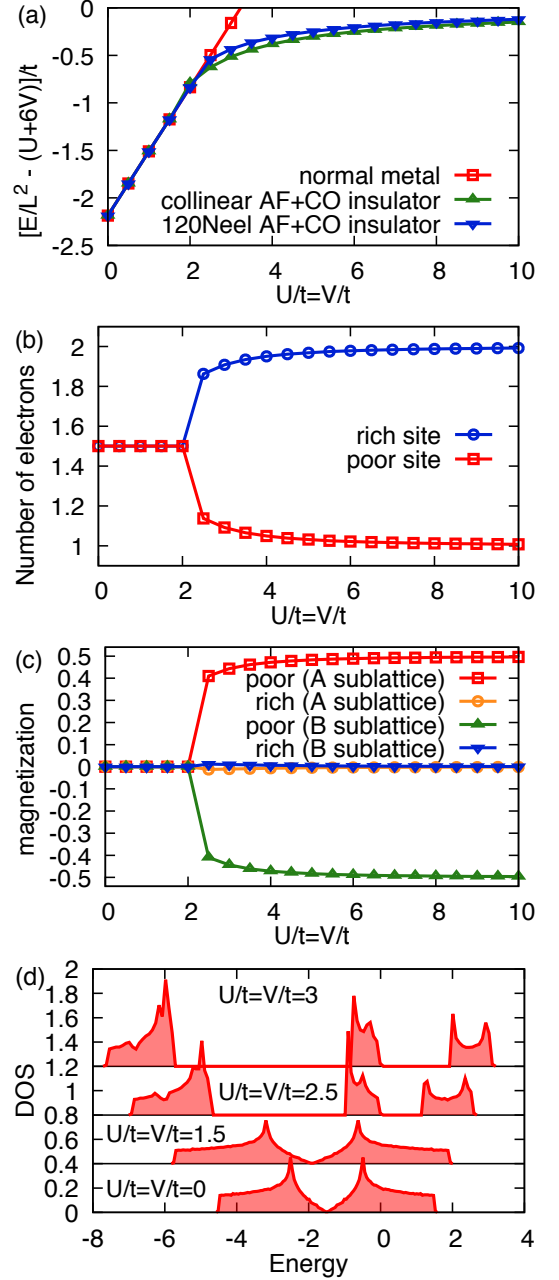


FIG. 7: (Color online) Results for the honeycomb lattice at $3/4$ filling for $U = V$ obtained by the Hartree-Fock method. (a) Energy of each state as a function of $U = V$. (b) The number of electrons per each sublattice for ground states (normal metal and charge ordered collinear AF state). (c) Magnetization of ground states. Charge-poor (charge-rich) sites show large (small) magnetization. (d) Density of states for the ground state. The Fermi level is set to 0.

$U < \infty$, the formation of intermediate double-occupied sites leads to other six cyclic process in K_3^{\triangleleft} and in K_3^{\triangleright} . Since P_3 can be mapped to two-spin exchange operators³⁵, these permutation terms finally result in ferromagnetic exchange interactions. The effective spin

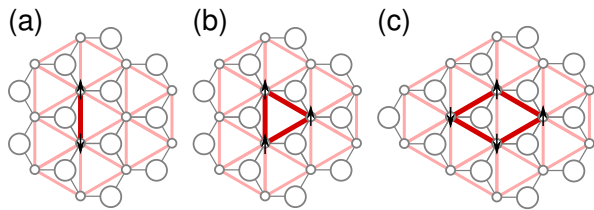


FIG. 8: (Color online) Illustration of effective (a) two-, (b) three- spin interaction terms of Eqs. (3) and (4) and (c) a four-site spin ring exchange.

Hamiltonian is given by

$$H = J_1^{\text{eff}} \sum_{\langle i,j \rangle_1} \mathbf{S}_i \cdot \mathbf{S}_j \quad (5)$$

with $J_1^{\text{eff}} = J_1 + 2K_3^c + 2K_3^d$.

In the limit $(V/t)^3 \gg U/t$, antiferromagnetic spin correlations become relevant ($J_1 \gg K_3$), and hence J_1^{eff} becomes antiferromagnetic. On the other hand, when $U/t \gg (V/t)^3$, antiferromagnetic spin correlations are suppressed ($K_3 \gg J_1$), leading to a ferromagnetic J_1^{eff} . This is consistent with the results in the previous section.

Furthermore, when $(V/t)^3 \sim U/t$, ferromagnetic K_3 and antiferromagnetic J_1 nearly cancel out. In this case, higher order processes in the perturbation theory become relevant. One of the dominant terms is a four-spin ring-exchange interaction $K_4(P_4 + P_4^{-1})$ on the effective triangular lattice, as shown in Figs. 8 (c) and A.4. This may induce exotic spin liquid states^{36–38} or chiral magnetic order^{39,40}. Moreover, the effective energy scale is extremely small ($|J_1^{\text{eff}}| \sim |K_4| \sim t^8/V^7$), which induces highly degenerate low-energy states.

D. Charge ordering vs. phase separation

The presence of charge order is a necessary condition for the validity of the perturbation expansion discussed in Sec. II C. The mean-field approach tends however to overestimate the stability range of ordered phases and to underestimate the stability of nonordered metallic phases stabilized in turn by quantum fluctuations. In what follows, we investigate the stability of the ordered state performing variational Monte Carlo simulations. We prepare the initial states by choosing the charge ordered states found in the restricted Hartree-Fock method and then optimize the variational parameters. The details of the method are presented in Appendix A.3.

The Hartree-Fock calculation suggests that a triangular-like charge order appears at large V . We first check with variational Monte Carlo (VMC) the stability when U as well as V are large. We confirm the presence of the insulating state with charge order and stripe antiferromagnetic order at $U/t = V/t = 10$. Both the number of electrons per orbital and the magnetization are nearly saturated as shown in Figs. 9(d)–9(f). The

momentum distribution $n(k)$ is a smooth function of k [Fig. 9(f)], suggesting the state to be insulating. Note that our variational wave function also finds a metallic state without charge and magnetic orders at $U/t = V/t = 2$ [see Figs. 9(a)–9(c)]. Figure 10 presents the schematic phase diagram for $V = U$ obtained with the various approaches considered here.

Besides, we do not find any indication of phase separation, which can be detected by the divergence of the charge structure factor $N(q)$ at the smallest achievable wave vector $q \sim 2\pi/L$ ⁴¹.

We now investigate the case of $U = 0$ and large V , namely, $V/t = 10, 20, 30$, with the VMC method. Note that perturbation theory is not applicable in this case since U is not large enough. When $V/t = 10$, the charge ordered metallic state found in the mean-field calculation is replaced by a metal without any charge order. The total charge structure factor $N(q)$, see Eq. (A52), shows q -linear behavior near $q \sim 0$, suggesting the state to be metallic.

On the other hand, when $V/t = 20$ and 30 , we find a charge disproportionate state, where the average number of c electrons is larger than that of d electrons. As shown in Fig. 11, $N(q)$ is found to have sharp peaks near $q \sim 2\pi/L$, suggesting phase separation⁴¹. The peaks in $N(q)$ appear to be dominated by that of the charge-poor d -orbital charge structure factor $N^{dd}(q)$; see Eq. (A51). This means that phase separation is mainly activated in the d -orbital sector.

In order to clarify the mechanism of phase separation, we also take a snapshot of this state. As shown in Fig. 12(a), phase separation is characterized by the charge ordered insulating state with a 2020... structure (doubly occupied–empty–doubly occupied–empty... sites) and the metallic state with a mixture of doubly occupied and singly occupied sites. Following the conventions⁴², we denote single-occupied sites with spin as “spinons” while doubly occupied (empty) sites with no spin as “doublons” (“holons”). For the charge-rich c orbital, each site is nearly doubly occupied and there are no holon sites (empty sites) [see Fig. 12(b)]. On the other hand, for the charge-poor d orbital there are two islands: one formed by holons and the other one that is a mixture of doublons and spinons [see Fig. 12(c)]. In this doublon-spinon mixture region, each spinon can hop through a doublon sea of the c and d orbitals. This does not cost an additional energy if two spinons are not next to each other on the original honeycomb lattice. Each spinon is always surrounded by three doublons, which reside on the nearest-neighbor sites of the honeycomb lattice. It can be assumed that one spinon and at least one doublon are bound together, and this new quasiparticle freely moves inside the doublon sea. The total kinetic energy gain is determined by the size of the doublon sea and the effective filling of the new quasiparticles. We note that the concept of spin-charge separation has been only rigorously defined in one spatial dimension; however, such a possibility has been also discussed in higher dimensions

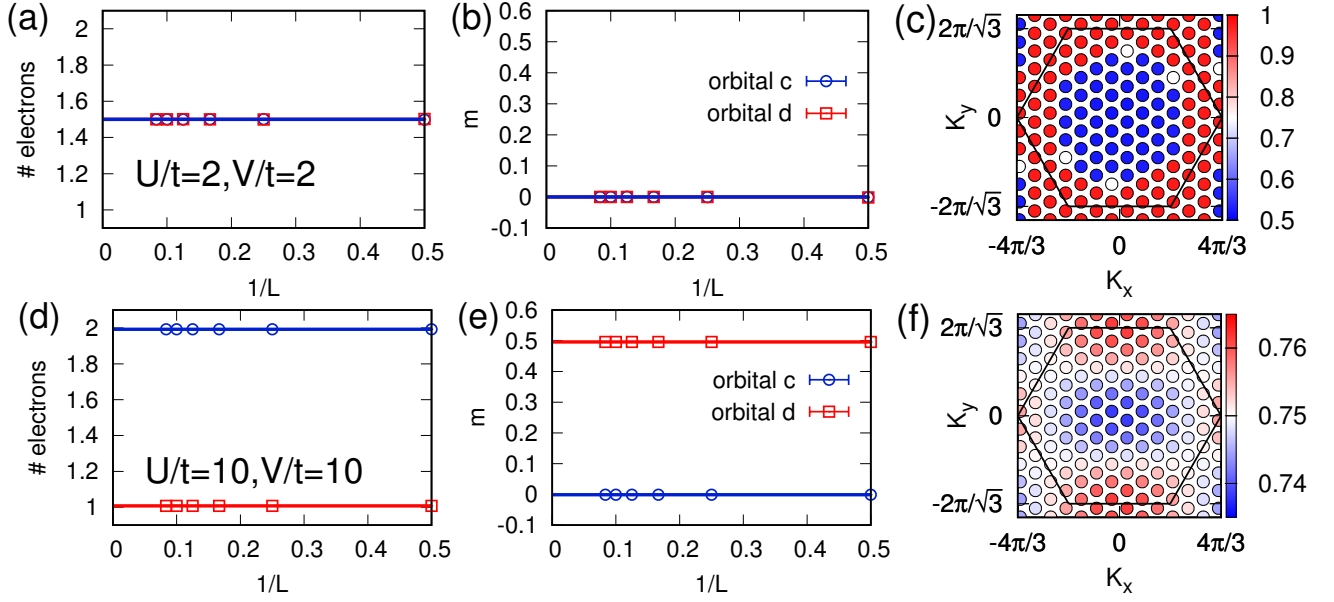


FIG. 9: (Color online) Variational Monte Carlo (symbols) and Hartree-Fock (lines) results for the nonmagnetic metallic state ($U/t = V/t = 2$, top row) and the charge-ordered antiferromagnetic insulating state [$U/t = V/t = 10$, bottom row; as illustrated in Fig. 2(d)]. In the first column [panels (a) and (d)] the number of electrons for the two sites making up the unit cell are given [denoted as c and d orbitals; compare Eq. (2)]. In the second column [panels (b) and (e)] the respective sublattice magnetizations. In the last column [panels (c) and (f)] the respective momentum distributions $n(k)$, as evaluated for 200 sites (using VMC) are presented. The hexagon denotes the Brillouin zone of the honeycomb lattice.

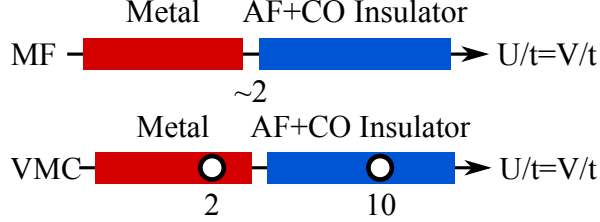


FIG. 10: (Color online) Schematic phase diagram for the honeycomb lattice at $3/4$ filling for $U = V$ obtained using Hartree-Fock (MF, top) and variational Monte Carlo (VMC, bottom).

in the presence of geometrical frustrations^{43,44}. Our numerical results imply that the system wants to generate a larger doublon sea with spinons to gain kinetic energy. This mechanism is similar to what has been found in the doped extended Hubbard model on a one-dimensional chain^{45,46} and a two-leg ladder⁴⁷.

Summarizing, a nearest-neighbor Coulomb interaction V at $U = 0$ stabilizes a charge ordered metal at the Hartree-Fock level. However inclusion of quantum fluctuations via the Gutzwiller approximation (GA), see Appendix A.2, and via finite-size VMC calculations suggests that the charge-ordered metal is replaced by phase separation, see Fig. 13, although the energies of these two states are found to be very close, as shown in Appendix B.2. Figure 13 shows the schematic phase diagram for $U = 0$ and finite V . We note that the critical

U is shifted to a larger value in the VMC result.

III. EMERGENT KAGOME AND CHAIN STRUCTURES ON A TRIANGULAR SYSTEM

In this section we investigate the extended Hubbard model on the isotropic triangular lattice, as defined by the Hamiltonian:

$$H = -t \sum_{\langle i,j \rangle, \sigma} c_{i,\sigma}^\dagger c_{j,\sigma} + \text{h.c.} + U \sum_i n_{i,\uparrow} n_{i,\downarrow} + V \sum_{\langle i,j \rangle} n_i n_j + V' \sum_{\langle\langle i,j \rangle\rangle} n_i n_j, \quad (6)$$

where t denotes the hopping parameter, U is the on-site Coulomb repulsion, V is the nearest-neighbor Coulomb interaction, and V' is the next-nearest-neighbor one. As in the previous section, we investigate repulsive Coulomb interactions, focusing on the appearance of charge-ordered states induced by a nonlocal potential. Here, we focus on $3/8$ filling ($n = 3/4$), where emergent kagome and one-dimensional structures may be generated by the appearance of charge order. Both effective lattices are shown in Fig. 14. When $U \gg V$, double occupancies are prohibited and the charge ordered ground state has a kagome-like structure, with three sites of the unit cell singly occupied and one site empty. By increasing the ratio V/U , the number of empty sites increases in order to avoid the energy loss from the V term, thus

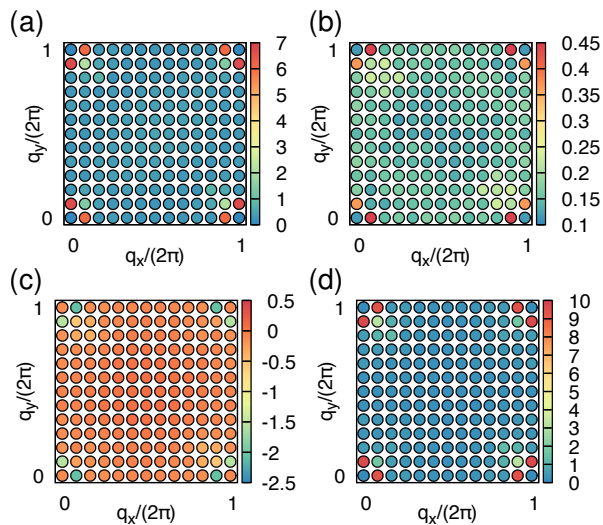


FIG. 11: (Color online) Charge structure factors at $(U/t, V/t) = (0, 30)$ (phase separated state) for the honeycomb lattice with 288 sites, as obtained by VMC. (a) Total charge structure factor $N(q)$. (b) Charge-rich orbital (*c*-orbital-*c*-orbital) charge structure factor $N^{cc}(q)$. (c) Charge structure factor between two different orbitals (*c*-orbital and *d*-orbital) $N^{cd}(q)$. (d) Charge-poor orbital (*d*-orbital-*d*-orbital) charge structure factor $N^{dd}(q)$. The total charge structure factor $N(q)$ shows sharp peaks at the achievable smallest wave vector q , suggesting phase separation. Since $N^{dd}(q_{\text{peak}}) \gg N^{cc}(q_{\text{peak}})$ and $N(q)$ is similar to the *d*-orbital (charge-poor orbital) charge structure factor $N^{dd}(q)$, phase separation mainly occurs in the *d*-orbital sector.

inducing a one-dimensional (1D) charge structure. We remark that the presence of a nearest-neighbor Coulomb repulsion is not sufficient to stabilize the aforementioned charge orders and one additional next-nearest neighbor V' is necessary in the triangular lattice case. Indeed, if we consider for example the kagome-like order of Fig. 14 (a), we can describe it as alternate rows that are fully occupied and rows where only half of the sites are occupied. If interaction is restricted to nearest neighbors, the reciprocal positions of the empty sites between different rows can be changed without any further energy cost, implying the absence of charge order in the system.

In the $t \rightarrow 0$ limit, the energy of the kagome and the 1D phases can be easily computed being equal to $E = 3/2(V + V')$ for the kagome substructure and to $E = V + V' + U/4$ for the 1D one. The 1D phase is then more favorable than the kagome one when $V + V' \geq U/2$. Here we set $U = 30$, in analogy with our former investigation of charge ordered phases on the triangular lattice⁴, and $V' = V/5$.

The model of Eq. (6) is studied by means of the variational Monte Carlo method, the details being presented in Appendix A.3. In order to distinguish the different kinds of charge ordering in the model, we plot in Fig. 15 the average electronic density per sublattice n_α , with $\alpha = A, B, C, D$ for each of the four sublattices that build

up the unit cell (see Fig. 14). Our results show that for $V/t \leq 5$, the charge is uniformly distributed in the lattice, while for $6 \leq V/t \leq 12$ one sublattice depletes, with the electrons forming an effective kagome lattice. In this case the frustration of the original lattice is effectively enhanced. Finally, as expected from the Coulomb energy argument, the 1D substructure of Fig. 14 is stabilized for $V/t \geq 13$.

As discussed also in the honeycomb lattice section, the static structure factor $N(q) = \langle n_q n_{-q} \rangle$ is a good indicator for metallic behavior. The metallic phase is characterized by $N(q) \propto |q|$ for $q \rightarrow 0$, which implies a vanishing gap for particle-hole excitations. On the contrary, $N(q) \propto q^2$ for $q \rightarrow 0$, implies a finite charge gap and insulating behavior^{4,48}. The results shown in Fig. 16 indicate that the system is metallic in the absence of charge order ($V/t = 4, 5$), while the charge ordered state with an effective kagome lattice exhibits an insulating behavior ($V/t = 6, 8, 10, 12$). $N(q)$ is shown along the path in the Brillouin zone connecting the point $\Gamma = (0, 0)$ to the point $M = (\pi, \pi/\sqrt{3})$ but a similar behavior can be obtained also along other directions. The results for the 1D charge ordered phase at $V/t = 13$ indicate also an insulating behavior although we observe a dependence on the path chosen in the Brillouin zone, with strong finite-size effects. By increasing the lattice size up to $L = 400$ we find, however, an insulating behavior along all the selected paths (not shown).

In a similar way, one can consider the small- q behavior of the spin-spin correlations $S(q) = \langle s_q s_{-q} \rangle$ to discriminate between a spin gapped and a spin gapless behavior. Our results indicate that the effective kagome lattice, induced by charge order, is characterized by gapless spin excitations, since $S(q) \propto |q|$ for $q \rightarrow 0$; see Fig. 17. Moreover, no peak can be observed in the spin-spin correlations, implying the absence of magnetic correlations, even at the short-range scale. We point out that gapless spin excitations have been also proposed for the Heisenberg model on the kagome lattice, by a similar variational approach⁴⁹, while the density matrix renormalization group approach suggests a finite gap in the spin excitations⁵⁰.

We finally summarize the VMC phase diagram of the model of Eq. (6) at $3/8$ filling, as a function of V/t , in Fig. 18.

IV. CONCLUSIONS

In conclusion, by using a combination of Hartree-Fock, perturbation theory, and variational Monte Carlo, we have investigated the possibility of novel lattice structures emerging from charge disproportionation in doped systems via strong correlations. In particular, we find an emergent geometrical frustration on bipartite honeycomb lattices, and an enhancement of the underlying geometrical frustration on a triangular lattice when Coulomb interactions beyond on-site are considered.

Concerning the honeycomb lattice, we have found that

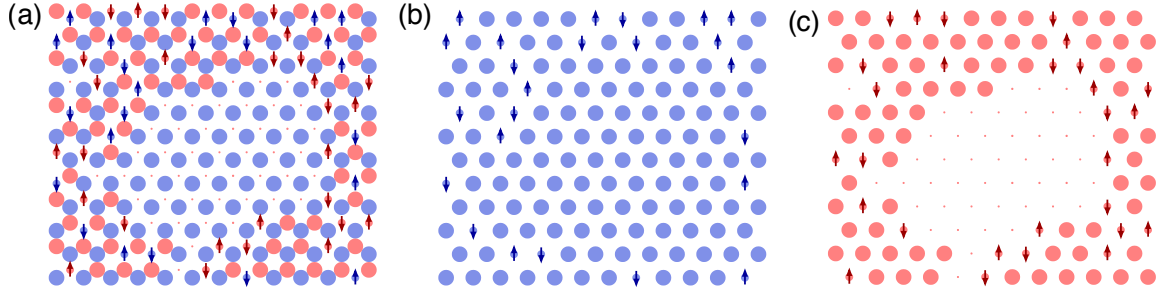


FIG. 12: (Color online) Snapshot of a phase separated state at $(U/t, V/t) = (0, 30)$ for 288 sites in the VMC calculation. Large and small circles correspond to doublons and spinons, respectively. Dots correspond to holons. Up and down arrows correspond to up and down spins, respectively. (a) Spin and charge configurations for both orbitals. (b) Same snapshot for only charge-rich c orbital. It mainly consists of doublons. (c) Same snapshot for only charge-poor d orbital. It consists of large doublon and holon islands.

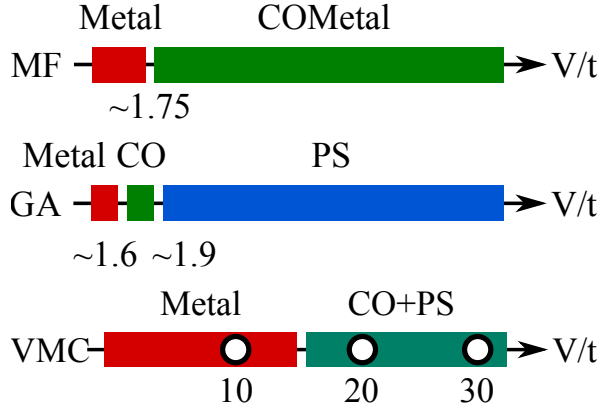


FIG. 13: (Color online) Schematic phase diagrams for the honeycomb lattice at $3/4$ filling and $U = 0$ obtained using restricted Hartree-Fock (MF, top), the Gutzwiller approximation (GA, middle) and variational Monte Carlo (VMC, bottom). CO denotes a charge ordered phase, while PS denotes a phase separated phase.

in the presence of both on-site U and nearest-neighbor V Coulomb interactions, charge order converts the original honeycomb structure at $3/4$ filling into an effective *half-filled* triangular lattice where the charge ordered state is characterized by a $2121\cdots$ ordered pattern, while the singly occupied sites have a macroscopic spin degeneracy. A nonzero hopping t lifts the spin degeneracy by forming magnetic order, which can be controlled by the Coulomb interactions U and V .

Our analysis via Hartree-Fock of charge order and spin correlations shows that most of the $U - V$ phase diagram at large values of U and V is characterized by a charge ordered antiferromagnetic insulator. This result is corroborated by VMC calculations for selected values of the parameter space. The emergent antiferromagnetic spin correlations are consistent with the effective antiferromagnetic Heisenberg model predicted by our perturbation theory analysis. When U is much larger than V , a charge ordered ferromagnetic insulating state appears instead, which is consistent with the results from per-

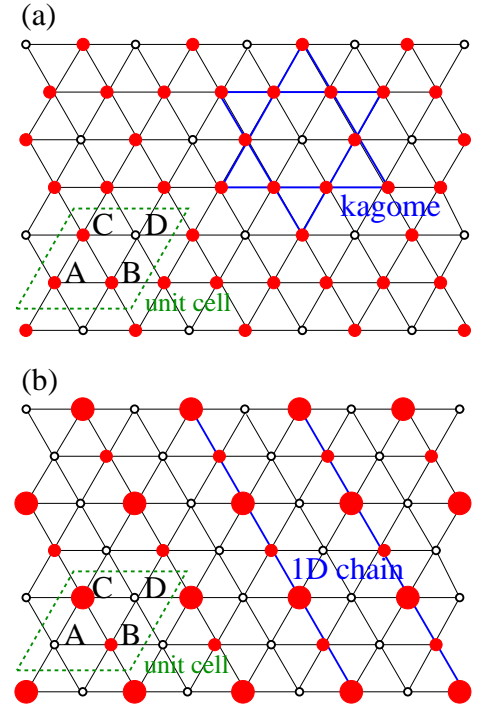


FIG. 14: (Color online) (a) Effective kagome lattice generated by charge order at $n = 3/4$ on the triangular lattice. The unit cell contains four sites and is denoted by a green parallelogram. Small empty circles denote empty sites, while full red circles denote single-occupied sites. (b) Effective 1D chains generated by charge order at $n = 3/4$ on the triangular lattice. Small empty circles denote empty sites, full small red circles denote single-occupied sites, while full large red circles denote double-occupied sites.

turbation theory. By further decreasing V , charge order completely disappears, and eventually a Nagaoka ferromagnetic semimetal⁵¹ appears for $V/t \gtrsim 6$.

For $U = 0$ and finite V , we find a charge ordered metal as the ground-state candidate. Inclusion of quantum fluctuations via the VMC method, as well as the Gutzwiller approximation, suggests however that this state may be

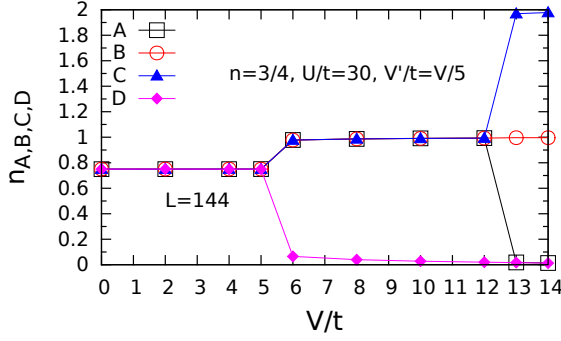


FIG. 15: (Color online) Electronic density n_α as a function of V/t obtained from VMC calculations for each of the four sublattices A , B , C , and D , as present in the effective lattices emerging from the charge ordered $n = 3/4$ triangular lattice, as illustrated in Fig. 14. The data are for $U/t = 30$, $V' = V/5$, and a lattice size $L = 144$.

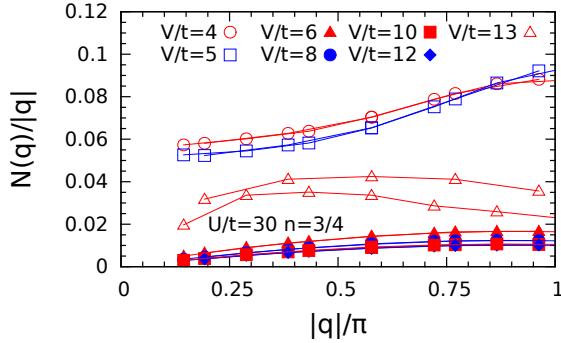


FIG. 16: (Color online) Variational Monte Carlo results for $N(q)/|q|$ as a function of $|q|/\pi$ for different values of V/t . The data are for $n = 3/4$ and $U/t = 30$ for the triangular lattice and for momenta q connecting $\Gamma = (0,0)$ and $M = (\pi, \pi/\sqrt{3})$. The results for lattice sizes $L = 144$ and $L = 256$ are superimposed.

unstable towards phase separation by forming a charge ordered insulating region and a metallic one.

Concerning the triangular lattice, we find that effective kagome and one-dimensional lattices are generated at $3/8$ filling ($n = 3/4$) because of the presence of charge order. We consider a large value of the on-site Coulomb repulsion U and a small, but finite, value of the next-nearest-neighbor Coulomb interaction $V' = V/5$. By increasing the ratio V/U above $V/U \simeq 5.5$, the uniform metallic phase evolves into an insulating state, where the electronic charges form a kagome structure, each site being singly occupied. The emergence of a kagome lattice out of the original triangular one effectively enhances the frustration of the original lattice. The behavior of the spin-spin correlations $S(q)$ shows that the effective kagome lattice generated by charge order is nonmagnetic, with gapless spin excitations. By further increasing the ratio V/U above $V/U \simeq 12.5$, the number of empty sites increases in order to avoid the energy loss due to the V

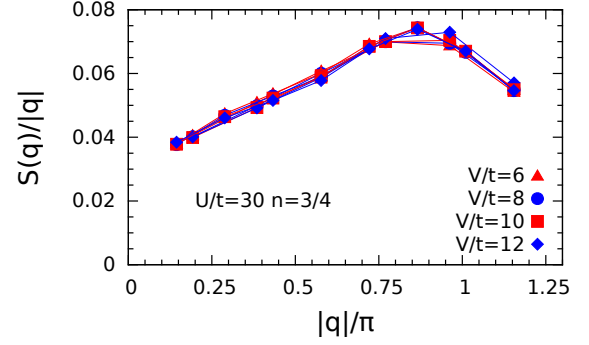


FIG. 17: (Color online) $S(q)/|q|$ as a function of $|q|/\pi$ for different values of V/t , within the region where the effective kagome lattice is stabilized. Data are shown along the line between $\Gamma = (0,0)$ and $M = (\pi, \pi/\sqrt{3})$ in the Brillouin zone on the $L = 144$ and the $L = 256$ lattice sizes.

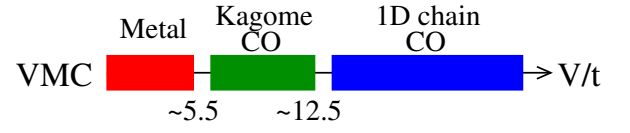


FIG. 18: (Color online) Schematic VMC phase diagram of the model of Eq. (6) as a function of V/t at $3/8$ filling, where we set $U/t = 30$ and $V' = V/5$. For $V/t \leq 5$ we observe a metallic phase with a uniform charge distribution. For $6 \leq V/t \leq 12$ we stabilize the charge ordered insulator with an effective kagome lattice of Fig. 14 (a). Finally, for $V/t \geq 13$, the charge ordered insulator with effective 1D chains of Fig. 14 (b) occurs.

term, thus generating another charge ordered insulator, where electrons form a one-dimensional charge structure.

Note added: Recently we became aware of a paper⁵² by Sugita and Motome that reports the emergence of kagome and one-dimensional charge orders on a triangular extended Hubbard model in the presence of spin-orbit coupling.

Acknowledgments

The authors would like to thank F. Becca, A. Kim, and S. M. Winter for fruitful discussions. R.K., R.V., and C.G. acknowledge the support of the German Science Foundation through Grant No. SFB/TRR49. L.F.T. acknowledges the support of the Italian Ministry of Education, University, and Research through Grant No. PRIN 2010 2010LLKJBX. The variational Monte Carlo code, which is used in the honeycomb lattice, is based on a code first developed by Tahara⁵³.

Appendix A: Theoretical methods

For the honeycomb lattice, we have analyzed the extended Hubbard model on the honeycomb lattice by (1)

the restricted Hartree-Fock method, (2) the Gutzwiller approximation, (3) the variational Monte Carlo (VMC) method, and (4) perturbation theory. For the extended Hubbard model (up to second neighbors) on the triangular lattice we have restricted ourselves to the VMC calculations. In this appendix we show the details of the methods.

A.1. Restricted Hartree-Fock method

We consider a system size of $N_s = 2N_{\text{dimer}} = 2L^2$.

The restricted Hartree-Fock approximation consists of a mean-field decoupling of the Hamiltonian of Eq. (2). The mean-field Hamiltonian up to constant terms is given as

$$\begin{aligned}
 H_{\text{MF}} = & \sum_{\mathbf{k},\sigma} \left(\epsilon_{\mathbf{k}} c_{\mathbf{k},\sigma}^\dagger d_{\mathbf{k},\sigma} + \epsilon_{\mathbf{k}}^* d_{\mathbf{k},\sigma}^\dagger c_{\mathbf{k},\sigma} \right) \\
 & + U \sum_{i,\sigma} \left(\langle n_{i,\sigma}^c \rangle n_{i,\bar{\sigma}}^c + \langle n_{i,\sigma}^d \rangle n_{i,\bar{\sigma}}^d \right) \\
 & + V \sum_i \left(\langle n_i^d \rangle n_i^c + \langle n_i^c \rangle n_i^d + \langle n_i^d \rangle n_{i+\mathbf{e}_x}^c \right. \\
 & + \langle n_{i+\mathbf{e}_x}^c \rangle n_i^d + \langle n_i^d \rangle n_{i+\mathbf{e}_y}^c + \langle n_{i+\mathbf{e}_y}^c \rangle n_i^d \\
 & - V \sum_{i,\sigma} \left(\langle d_{i,\sigma}^\dagger c_{i,\sigma} \rangle c_{i,\sigma}^\dagger d_{i,\sigma} \right. \\
 & + \langle d_{i,\sigma}^\dagger c_{i+\mathbf{e}_x,\sigma} \rangle c_{i+\mathbf{e}_x,\sigma}^\dagger d_{i,\sigma} \\
 & + \langle d_{i,\sigma}^\dagger c_{i+\mathbf{e}_y,\sigma} \rangle c_{i+\mathbf{e}_y,\sigma}^\dagger d_{i,\sigma} + \text{h.c.} \left. \right), \quad (\text{A1})
 \end{aligned}$$

$$\epsilon_{\mathbf{k}} = -t(1 + e^{-ik_x} + e^{-ik_y}), \quad (\text{A2})$$

$$n_i^\alpha = n_{i,\uparrow}^\alpha + n_{i,\downarrow}^\alpha \quad (\alpha = c, d). \quad (\text{A3})$$

For a collinear state, we assume

$$\langle n_{i,\sigma}^c \rangle = n_\sigma^c + (-1)^{R_i} \delta n_\sigma^c, \quad (\text{A4})$$

$$\langle n_{i,\sigma}^d \rangle = n_\sigma^d + (-1)^{R_i} \delta n_\sigma^d, \quad (\text{A5})$$

$$\langle d_{i,\sigma}^\dagger c_{i,\sigma} \rangle = \chi_\sigma + (-1)^{R_i} \delta \chi_\sigma, \quad (\text{A6})$$

$$\langle d_{i,\sigma}^\dagger c_{i+\mathbf{e}_x,\sigma} \rangle = \langle d_{i,\sigma}^\dagger c_{i+\mathbf{e}_y,\sigma} \rangle \quad (\text{A7})$$

$$= \eta_\sigma + (-1)^{R_i} \delta \eta_\sigma, \quad (\text{A8})$$

which contains 16 independent parameters. Here, $(-1)^{R_i} = e^{i\mathbf{Q} \cdot \mathbf{R}_i}$ with the momentum $\mathbf{Q} = (\pi, \pi)$ for a 2×2 sublattice. We can rewrite the Hamiltonian as

$$\begin{aligned}
 H_{\text{MF}} = & \sum_{\mathbf{k},\sigma} \begin{pmatrix} c_{\mathbf{k},\sigma}^\dagger & c_{\mathbf{k}+\mathbf{Q},\sigma}^\dagger & d_{\mathbf{k},\sigma}^\dagger & d_{\mathbf{k}+\mathbf{Q},\sigma}^\dagger \end{pmatrix} \\
 & \begin{pmatrix} O_{c,\sigma} & \Delta_{c,\sigma} & \tilde{\epsilon}_{\mathbf{k},\sigma} & Y_{\mathbf{k},\sigma} \\ \Delta_{c,\sigma} & O_{c,\sigma} & Y_{\mathbf{k}+\mathbf{Q},\sigma} & \tilde{\epsilon}_{\mathbf{k}+\mathbf{Q},\sigma} \\ \tilde{\epsilon}_{\mathbf{k},\sigma}^* & Y_{\mathbf{k}+\mathbf{Q},\sigma}^* & O_{d,\sigma} & \Delta_{d,\sigma} \\ Y_{\mathbf{k},\sigma}^* & \tilde{\epsilon}_{\mathbf{k}+\mathbf{Q},\sigma}^* & \Delta_{d,\sigma} & O_{d,\sigma} \end{pmatrix} \begin{pmatrix} c_{\mathbf{k},\sigma} \\ c_{\mathbf{k}+\mathbf{Q},\sigma} \\ d_{\mathbf{k},\sigma} \\ d_{\mathbf{k}+\mathbf{Q},\sigma} \end{pmatrix} \quad (\text{A9})
 \end{aligned}$$

with

$$O_{c,\sigma} = Un_\sigma^c + 3V(n_\uparrow^d + n_\downarrow^d), \quad (\text{A10})$$

$$O_{d,\sigma} = Un_\sigma^d + 3V(n_\uparrow^c + n_\downarrow^c), \quad (\text{A11})$$

$$\Delta_{c,\sigma} = U\delta n_\sigma^c - V(\delta n_\uparrow^d + \delta n_\downarrow^d), \quad (\text{A12})$$

$$\Delta_{d,\sigma} = U\delta n_\sigma^d - V(\delta n_\uparrow^c + \delta n_\downarrow^c), \quad (\text{A13})$$

$$\tilde{\epsilon}_{\mathbf{k},\sigma} = \epsilon_{\mathbf{k}} - V[\chi_\sigma + \eta_\sigma(e^{-ik_x} + e^{-ik_y})], \quad (\text{A14})$$

$$Y_{\mathbf{k},\sigma} = -V[\delta\chi_\sigma + \delta\eta_\sigma(e^{-ik_x} + e^{-ik_y})]. \quad (\text{A15})$$

We further diagonalize the Hamiltonian and determine the above parameters self-consistently. The self-consistent equations are given by

$$n_\sigma^c = \frac{1}{N} \sum_{\mathbf{k}}^{\text{RBZ}} \left[\langle c_{\mathbf{k},\sigma}^\dagger c_{\mathbf{k},\sigma} \rangle + \langle c_{\mathbf{k}+\mathbf{Q},\sigma}^\dagger c_{\mathbf{k}+\mathbf{Q},\sigma} \rangle \right], \quad (\text{A16})$$

$$n_\sigma^d = \frac{1}{N} \sum_{\mathbf{k}}^{\text{RBZ}} \left[\langle d_{\mathbf{k},\sigma}^\dagger d_{\mathbf{k},\sigma} \rangle + \langle d_{\mathbf{k}+\mathbf{Q},\sigma}^\dagger d_{\mathbf{k}+\mathbf{Q},\sigma} \rangle \right], \quad (\text{A17})$$

$$\delta n_\sigma^c = \frac{1}{N} \sum_{\mathbf{k}}^{\text{RBZ}} \left[\langle c_{\mathbf{k},\sigma}^\dagger c_{\mathbf{k}+\mathbf{Q},\sigma} \rangle + \langle c_{\mathbf{k}+\mathbf{Q},\sigma}^\dagger c_{\mathbf{k},\sigma} \rangle \right], \quad (\text{A18})$$

$$\delta n_\sigma^d = \frac{1}{N} \sum_{\mathbf{k}}^{\text{RBZ}} \left[\langle d_{\mathbf{k},\sigma}^\dagger d_{\mathbf{k}+\mathbf{Q},\sigma} \rangle + \langle d_{\mathbf{k}+\mathbf{Q},\sigma}^\dagger d_{\mathbf{k},\sigma} \rangle \right], \quad (\text{A19})$$

$$\chi_\sigma = \frac{1}{N} \sum_{\mathbf{k}}^{\text{RBZ}} \left[\langle d_{\mathbf{k},\sigma}^\dagger c_{\mathbf{k},\sigma} \rangle + \langle d_{\mathbf{k}+\mathbf{Q},\sigma}^\dagger c_{\mathbf{k}+\mathbf{Q},\sigma} \rangle \right], \quad (\text{A20})$$

$$\delta\chi_\sigma = \frac{1}{N} \sum_{\mathbf{k}}^{\text{RBZ}} \left[\langle d_{\mathbf{k},\sigma}^\dagger c_{\mathbf{k}+\mathbf{Q},\sigma} \rangle + \langle d_{\mathbf{k}+\mathbf{Q},\sigma}^\dagger c_{\mathbf{k},\sigma} \rangle \right], \quad (\text{A21})$$

$$\eta_\sigma = \frac{1}{N} \sum_{\mathbf{k}}^{\text{RBZ}} \left[e^{ik_x} \langle d_{\mathbf{k},\sigma}^\dagger c_{\mathbf{k},\sigma} \rangle \right. \quad (\text{A22})$$

$$\left. - e^{ik_x} \langle d_{\mathbf{k}+\mathbf{Q},\sigma}^\dagger c_{\mathbf{k}+\mathbf{Q},\sigma} \rangle \right], \quad (\text{A23})$$

$$\delta\eta_\sigma = \frac{1}{N} \sum_{\mathbf{k}}^{\text{RBZ}} \left[e^{ik_x} \langle d_{\mathbf{k}+\mathbf{Q},\sigma}^\dagger c_{\mathbf{k},\sigma} \rangle \right. \quad (\text{A24})$$

$$\left. - e^{ik_x} \langle d_{\mathbf{k},\sigma}^\dagger c_{\mathbf{k}+\mathbf{Q},\sigma} \rangle \right], \quad (\text{A25})$$

with $N = L^2$ being the number of \mathbf{k} points in the Brillouin zone. The ground states are obtained by filling the lowest-energy orbitals up to the number of electrons. We employ an antiperiodic-periodic boundary condition, and set the number of \mathbf{k} points as 120×120 .

Each state is characterized by the magnetization and the number of electrons for orbitals c and d , which are defined as

$$\langle S^{z,\alpha} \rangle = \frac{1}{N_{\text{dimer}}} \sum_i (-1)^{R_i} \langle S_i^{z,\alpha} \rangle, \quad (\text{A26})$$

$$\langle n^\alpha \rangle = \frac{1}{N_{\text{dimer}}} \sum_i \langle n_i^\alpha \rangle \quad (\alpha = c, d). \quad (\text{A27})$$

Similarly, for spiral states, we consider momentum $\mathbf{Q} = (-2\pi/3, 2\pi/3)$ for a 6-site sublattice, namely, the order parameters are given as $\langle n_{i,\sigma}^c \rangle = n_c$, $\langle n_{i,\sigma}^d \rangle = n_d (< n_c)$, $\langle c_{i,\uparrow}^\dagger c_{i,\downarrow}^\dagger \rangle = m_c e^{i\mathbf{Q} \cdot \mathbf{R}_i}$ with $m_c = 0$ (for charge-rich

sites), $\langle d_{i,\uparrow}^\dagger d_{i,\downarrow}^\dagger \rangle = m_d e^{i\mathbf{Q} \cdot \mathbf{R}_i}$ with $m_d \neq 0$ (for charge-poor sites), $\langle d_{i,\sigma}^\dagger c_{i,\sigma}^\dagger \rangle = \chi$, and $\langle d_{i,\sigma}^\dagger c_{i+\mathbf{e}_x(\mathbf{e}_y),\sigma}^\dagger \rangle = \eta$, and the corresponding reduced Brillouin zone.

We also calculate the gap in the density of states at the Fermi level to check whether the state is metallic or insulating.

A.2. Gutzwiller approximation

We applied the Gutzwiller approximation to the extended Hubbard model on the honeycomb lattice. In the Gutzwiller approximation, the nearest-neighbor correlations $\langle T_{cd\sigma} \rangle = \langle c_{i,\sigma}^\dagger d_{j,\sigma} \rangle$ in the correlated wave function $|\psi\rangle$ are evaluated via those in the uncorrelated wave function $|\psi\rangle_0$ through the renormalization factor $\eta_{cd\sigma}$ ^{54,55}:

$$\langle c_{i,\sigma}^\dagger d_{j,\sigma} \rangle = \eta_{cd\sigma} \langle c_{i,\sigma}^\dagger d_{j,\sigma} \rangle_0. \quad (\text{A28})$$

The matrix elements of $c_{i,\sigma}^\dagger d_{j,\sigma}$ in the uncorrelated wave function $|\psi\rangle_0$ are proportional to

$$\sqrt{n_{c\sigma}^0(1-n_{c\sigma}^0)} \sqrt{n_{d\sigma}^0(1-n_{d\sigma}^0)}. \quad (\text{A29})$$

Here, $n_{c\sigma}^0 = n_{d\sigma}^0 = 3/4$ at $3/4$ filling. Generalizing this to the matrix elements of the correlated state, we find

$$\eta_{cd\sigma} = \frac{(\sqrt{h_c s_{c\sigma}} + \sqrt{s_{c\bar{\sigma}} d_c})(\sqrt{s_{d\sigma} h_d} + \sqrt{d_d s_{d\bar{\sigma}}})}{\sqrt{n_{c\sigma}^0(1-n_{c\sigma}^0)} \sqrt{n_{d\sigma}^0(1-n_{d\sigma}^0)}}. \quad (\text{A30})$$

for the Gutzwiller approximation of the kinetic energy term $T_{cd\sigma}$. We define occupancies for empty (h), singly (s), and doubly (d) occupied sites for orbital c (similarly for orbital d):

$$h_c = \langle (1 - c_\uparrow^\dagger c_\uparrow)(1 - c_\downarrow^\dagger c_\downarrow) \rangle, \quad (\text{A31})$$

$$s_{c\sigma} = \langle c_\sigma^\dagger c_\sigma (1 - c_{\bar{\sigma}}^\dagger c_{\bar{\sigma}}) \rangle, \quad (\text{A32})$$

$$d_c = \langle c_\uparrow^\dagger c_\uparrow c_\downarrow^\dagger c_\downarrow \rangle. \quad (\text{A33})$$

The expectation value of the nearest-neighbor Coulomb interaction is given as

$$\langle (c_\uparrow^\dagger c_\uparrow + c_\downarrow^\dagger c_\downarrow)(d_\uparrow^\dagger d_\uparrow + d_\downarrow^\dagger d_\downarrow) \rangle = (n_{c\uparrow} + n_{c\downarrow})(n_{d\uparrow} + n_{d\downarrow}). \quad (\text{A34})$$

The energy per bond in the Gutzwiller approximation is finally given as

$$E = -t \sum_{\sigma} \eta_{cd\sigma} \langle T_{cd\sigma} + T_{dc\sigma} \rangle_0 + \frac{U}{3} (d_c + d_d) + V (n_{c\uparrow} + n_{c\downarrow})(n_{d\uparrow} + n_{d\downarrow}). \quad (\text{A35})$$

The $1/3$ factor in the U term comes from the number of nearest-neighbor bonds per site. Here, the expectation value of the hopping is a function of $n_{c\sigma} + n_{d\sigma}$, and is defined as

$$-t \langle T_{cd\sigma} + T_{dc\sigma} \rangle_0 = \frac{1}{N_{\text{bond}}} \sum_{|k| < k_F^{\sigma}} \epsilon_k \quad (\text{A36})$$

with $N_{\text{bond}} = 3L^2$. Besides, the renormalization factor $\eta_{cd\sigma}$ is a function of $h_{c(d)}$, $s_{c(d)\sigma}$, and $d_{c(d)}$. One can eliminate the spinon $s_{c\sigma}$ and the holon h_c using

$$s_{c\sigma} = n_{c\sigma} - d_c, \quad (\text{A37})$$

$$h_c = 1 - s_{c\uparrow} - s_{c\downarrow} - d_c = 1 - n_{c\uparrow} - n_{c\downarrow} + d_c. \quad (\text{A38})$$

Therefore, the energy becomes a function of the parameters $n_{c\sigma}$, $n_{d\sigma}$, d_c , and d_d .

Naively, the energy minimum can be obtained by the condition

$$\frac{\partial E}{\partial d_c} = \frac{\partial E}{\partial d_d} = 0. \quad (\text{A39})$$

In the absence of on-site Coulomb interaction ($U = 0$), this yields

$$d_c = n_{c\uparrow} n_{c\downarrow}, \quad (\text{A40})$$

$$d_d = n_{d\uparrow} n_{d\downarrow}. \quad (\text{A41})$$

The expectation value of the doublon is a simple product of the number of up and down spins. This simplifies the renormalization factor:

$$\eta_{cd\sigma} = \frac{\sqrt{n_{c\sigma}(1-n_{c\sigma})} \sqrt{n_{d\sigma}(1-n_{d\sigma})}}{\sqrt{n_{c\sigma}^0(1-n_{c\sigma}^0)} \sqrt{n_{d\sigma}^0(1-n_{d\sigma}^0)}}. \quad (\text{A42})$$

Now, the energy is a function of a few parameters, namely, $n_{c\sigma}$ and $n_{d\sigma}$. The energy minimum can be searched analytically. For $U \neq 0$, however, the stationary condition does not give us simple conditions. We, instead, numerically find the energy minimum by controlling parameters $n_{c\sigma}$, $n_{d\sigma}$, d_c , and d_d .

A.3. Variational Monte Carlo method

As a third method which includes the effects of quantum fluctuations beyond mean field, we consider the variational Monte Carlo (VMC) technique. We use the Jastrow-Slater wave functions which allow metallic and insulating states with charge and antiferromagnetic orders. For the honeycomb lattice Eq. (2), we define

$$|\psi\rangle = P_{\text{CJ}} P_{\text{SJ}} |\phi\rangle, \quad (\text{A43})$$

$$|\phi\rangle = \left[\sum_{ij} (f_{ij}^{cc} c_{i,\uparrow}^\dagger c_{j,\downarrow}^\dagger + f_{ij}^{cd} c_{i,\uparrow}^\dagger d_{j,\downarrow}^\dagger + f_{ij}^{dc} d_{i,\uparrow}^\dagger c_{j,\downarrow}^\dagger + f_{ij}^{dd} d_{i,\uparrow}^\dagger d_{j,\downarrow}^\dagger) \right]^{N_e/2} |0\rangle, \quad (\text{A44})$$

$$f_{ij} = \begin{cases} f^A(\mathbf{r}_j - \mathbf{r}_i) & i \in \text{A sublattice}, \\ f^B(\mathbf{r}_j - \mathbf{r}_i) & i \in \text{B sublattice}, \end{cases} \quad (\text{A45})$$

$$P_{\text{CJ}} = \exp \left[\frac{1}{2} \sum_{ij} (v_{ij}^{\text{CJ},cc} n_i^c n_j^c + v_{ij}^{\text{CJ},cd} n_i^c n_j^d + v_{ij}^{\text{CJ},dd} n_i^d n_j^d) \right], \quad (\text{A46})$$

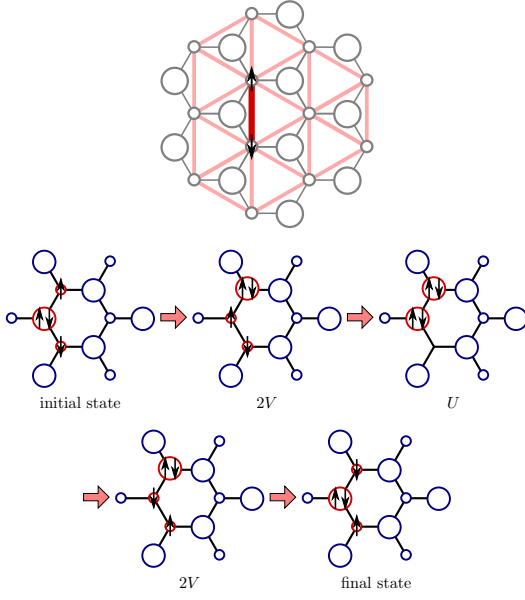


FIG. A.1: (Color online) Virtual hopping process which generates an effective nearest-neighbor spin exchange interaction between the triangular lattice sites emerging from the charge ordered $n = 3/2$ honeycomb lattice. Compare Eq. (A54).

$$P_{\text{SJ}} = \exp \left[2 \sum'_{ij} \left(v_{ij}^{\text{SJ},cc} S_i^{z,c} S_j^{z,c} + v_{ij}^{\text{SJ},cd} S_i^{z,c} S_j^{z,d} + v_{ij}^{\text{SJ},dd} S_i^{z,d} S_j^{z,d} \right) \right], \quad (\text{A47})$$

$$v_{ij}^{\text{SJ}} = v^{\text{SJ}}(|\mathbf{r}_j - \mathbf{r}_i|), \quad (\text{A48})$$

$$v_{ij}^{\text{CJ}} = v^{\text{CJ}}(|\mathbf{r}_j - \mathbf{r}_i|). \quad (\text{A49})$$

Here, \sum'_{ij} denotes a sum over $i \neq j$. We prepare the Slater part $|\phi\rangle$ by taking the Hartree-Fock solutions as initial states, and optimize the variational parameters f_{ij} , v_{ij}^{SJ} , and v_{ij}^{CJ} .

We use Eqs. (A26) and (A27) to characterize each phase. In order to see whether the phase is metallic or insulating, we calculate the total momentum distribution:

$$n(k) = \frac{1}{2N_s} \sum_{ij\sigma} \langle c_{i,\sigma}^\dagger c_{j,\sigma} + d_{i,\sigma}^\dagger d_{j,\sigma} \rangle e^{ik \cdot (r_i - r_j)}, \quad (\text{A50})$$

and the density-density structure factors for two orbitals:

$$N^{\alpha\beta}(q) = \frac{1}{N_{\text{dimer}}} \sum_{i,j} \langle n_i^\alpha n_j^\beta \rangle e^{iq \cdot (r_i - r_j)} \quad (\alpha = c, d). \quad (\text{A51})$$

Metallic states are detected by the jump of the momentum distribution $n(k)$ and q -linear behavior of the total charge structure factor

$$N(q) = N^{cc}(q) + N^{cd}(q) + N^{dc}(q) + N^{dd}(q) \quad (\text{A52})$$

near $q \sim 0$. On the other hand, $n(k)$ is smooth and $N(q) \sim q^2$ ($q \sim 0$) for insulating states.

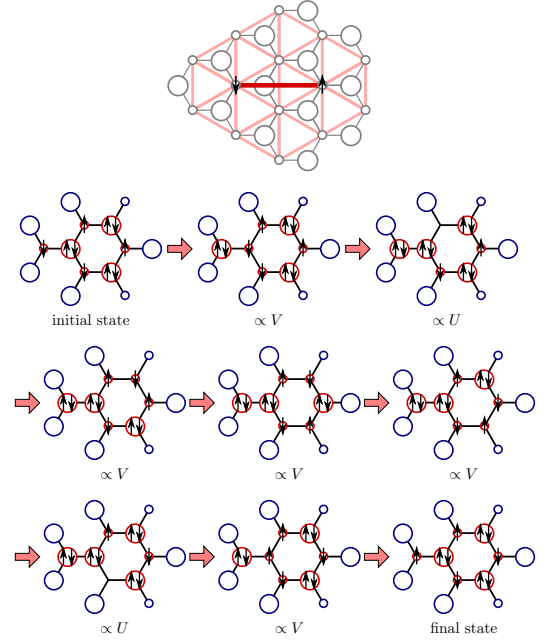


FIG. A.2: (Color online) Virtual hopping process which generates an effective next-nearest-neighbor spin exchange interaction between the triangular lattice sites emerging from the charge ordered $n = 3/2$ honeycomb lattice. Compare Eq. (A54).

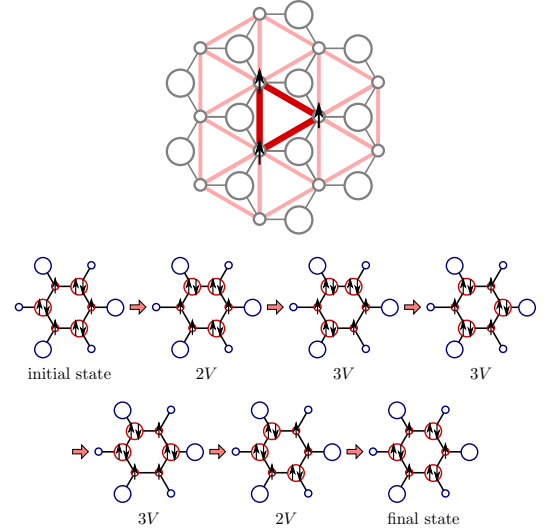


FIG. A.3: (Color online) Virtual hopping process which generates an effective three-spin permutation K_3^{\triangleright} (surviving even in the limit $U \rightarrow \infty$) between the triangular lattice sites emerging from the charge ordered $n = 3/2$ honeycomb lattice. Compare Eq. (A54).

Analogously, in order to simulate the triangular lattice model of Eq. (6), we have used the variational Monte Carlo method based on the variational ansatz $|\Psi\rangle = P_{\text{CJ}}|\text{FS}\rangle^{55-57}$, where $|\text{FS}\rangle$ is the noninteracting filled Fermi sea, to which a finite small superconductive term is added in order to regularize the wave function,

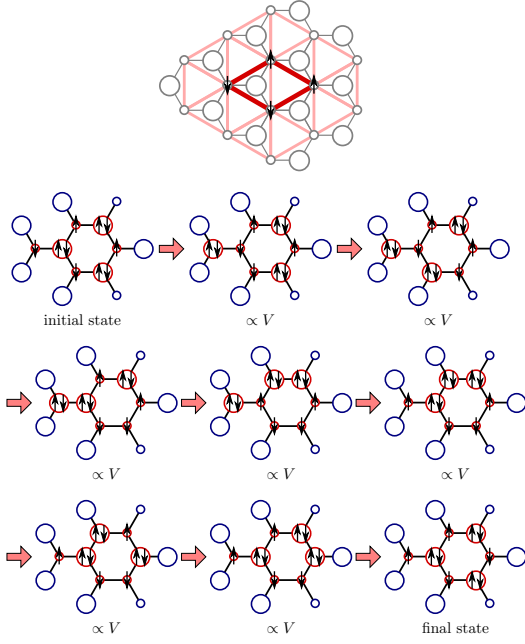


FIG. A.4: (Color online) Virtual hopping process which generates an effective four-spin permutation between the triangular lattice sites emerging from the charge ordered $n = 3/2$ honeycomb lattice. Compare Eq. (A54).

i.e., to separate the highest occupied and the lowest unoccupied states by a gap. The term

$$P_{\text{CJ}} = \exp \left(-\frac{1}{2} \sum_{i,j} v_{ij} n_i n_j \right) \quad (\text{A53})$$

is the density-density Jastrow factor⁵⁷, where the v_{ij} 's are optimized with variational Monte Carlo calculations for every independent distance $|\mathbf{r}_i - \mathbf{r}_j|$ (including on site). In order to investigate the formation of charge-ordered phases, we include four different chemical potentials in $|\text{FS}\rangle$, as variational parameters, one for each site of the unit cell, similarly to what has been done in Ref. 4. We tested that inclusion of backflow correlations to further improve the correlated state $|\Psi\rangle$ ^{48,58} is not crucial to describe charge-ordered states. All results presented here are obtained by optimizing individually⁵⁹ every variational parameter in the wave function and then performing a Monte Carlo sampling of the observables over the optimal state. The error bars are not shown since they are always smaller than the symbol size.

A.4. Details of the perturbation calculations on honeycomb systems

On the honeycomb lattice, when $U = V = \infty$, we expect a triangular charge order at $3/4$ filling ($n = 3/2$). Charge-rich sites contain two electrons per site, and do not have any left spin degrees of freedom. On the other

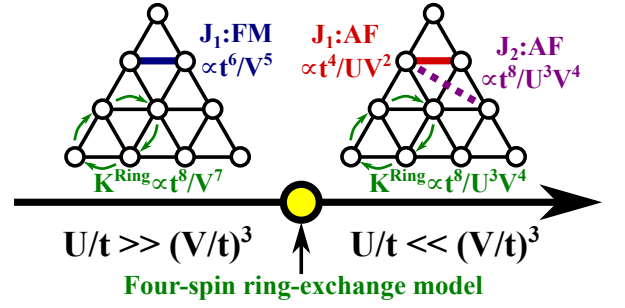


FIG. A.5: (Color online) Effective Hamiltonians for the triangular lattice emerging from the charge ordered $n = 3/2$ honeycomb lattice, see Eq. (A58), as a function of U/t and V/t .

hand, charge-poor sites contain one electron per site, and possess macroscopic spin degeneracy. The ground-state degeneracy is lifted in the presence of hopping t . From perturbation theory, the effective Hamiltonian can be obtained as a sum of the Heisenberg spin exchange and permutation terms:

$$\begin{aligned} H = & \sum_{\langle i,j \rangle_1} J_1 \left(\mathbf{S}_i \cdot \mathbf{S}_j - \frac{1}{4} \right) \\ & + \sum_{\langle i,j \rangle_2} J_2 \left(\mathbf{S}_i \cdot \mathbf{S}_j - \frac{1}{4} \right) + \dots \\ & + \sum_{\triangleright} K_3^{\triangleright} (P_3 + P_3^{-1}) \\ & + \sum_{\triangleleft} K_3^{\triangleleft} (P_3 + P_3^{-1}) \\ & + \sum_{\square} K_4 (P_4 + P_4^{-1}) + \dots \end{aligned} \quad (\text{A54})$$

For the spin exchange terms the sum is taken over all nearest-neighbor (next-nearest-neighbor) sites on an effective triangular lattice for $\langle i,j \rangle_1$ ($\langle i,j \rangle_2$). On the other hand, for the permutation terms, the sum is taken over all right-pointing (left-pointing) triangles which are located inside (outside) of hexagons for \triangleright (\triangleleft) and all squares for \square . The symbol P_n denotes a cyclic permutation operator.

Unlike the perturbation expansion in the triangular and kagome systems where electrons can hop odd times in local triangles, spin exchange interactions appear through only an even number of electron hoppings. Besides, the spin degeneracy is first lifted by a four virtual hopping process rather than a conventional two hopping process. For example, as shown in Fig. A.1, nearest-neighbor exchange on the triangular lattice appears through four hopping processes. The intermediate states have energy $2V$, U , and $2V$, respectively. There are four different ways of exchanging spins. This gives antiferromagnetic exchange $J_1 = 4t^4/[(2V)^2U] = t^4/(V^2U)$. Similarly, next-nearest-neighbor exchange on the triangular lattice is given as $J_2 = c_2 t^8/(V^5 U^2) + c_2' t^8/(V^4 U^3)$

with c_2, c'_2 being positive constants (see Fig. A.2). These exchange interactions are always antiferromagnetic:

$$J \propto \frac{t^{2n}}{\text{Coulomb interaction}^{2n-1}} > 0, \quad (\text{A55})$$

which results in strong geometrical frustration. They are similar to what has been found in the quarter-filled extended Hubbard models on a two-leg ladder⁴⁷ and a square lattice⁶⁰.

Analogously to spin exchange interactions, permutation terms in the present system always appear through an even number of virtual processes. As shown in Fig. A.3, three-site permutation terms appear through six cyclic processes, namely, $K_3^\triangleright = -d_3 t^6/V^5 + d_3' t^6/(V^4 U)$ [$K_3^\triangleleft = d_3'' t^6/(V^3 U^2)$] for triangles in (out of) hexagons with d_3, d_3' , and d_3'' being positive constants. Note that $K_3^\triangleright = -d_3 t^6/V^5$ survives even when $U = \infty$, which gives ferromagnetic interactions. Moreover, four-site permutation terms appear through eight cyclic processes as shown in Fig. A.4, namely, $K_4 = d_4 t^8/V^7 + d_4' t^8/(V^6 U) + d_4'' t^8/(V^5 U^2) + d_4''' t^8/(V^4 U^3)$ with d_4, d_4', d_4'' , and d_4''' being constants.

Since the three-spin permutation operator can be written as a product of two exchange operators

$$P_3 = P_{ijk} = P_{ij} P_{ik} = \frac{1}{4} (1 + 4 \mathbf{S}_i \cdot \mathbf{S}_j) (1 + 4 \mathbf{S}_i \cdot \mathbf{S}_k) \quad (\text{A56})$$

these terms become nearest-neighbor exchange interactions on the effective triangular lattice³⁵

$$P_3 + P_3^{-1} = \frac{1}{2} (1 + 4 \mathbf{S}_i \cdot \mathbf{S}_j + 4 \mathbf{S}_j \cdot \mathbf{S}_k + 4 \mathbf{S}_k \cdot \mathbf{S}_i). \quad (\text{A57})$$

K_3^\triangleright and K_3^\triangleleft will be renormalized into J_1 , and the Hamiltonian up to the constant term is rewritten as

$$H = \sum_{\langle i,j \rangle_1} J_1^{\text{eff}} \mathbf{S}_i \cdot \mathbf{S}_j + \sum_{\langle i,j \rangle_2} J_2 \mathbf{S}_i \cdot \mathbf{S}_j + \dots + \sum_{\square} K_4 (P_4 + P_4^{-1}) + \dots \quad (\text{A58})$$

Here, J_1^{eff} is a linear combination of J_1, K_3^\triangleright , and K_3^\triangleleft , namely, $J_1^{\text{eff}} = J_1 + 2K_3^\triangleright + 2K_3^\triangleleft$.

The effective nearest-neighbor interaction J_1^{eff} can be both ferromagnetic and antiferromagnetic depending on the size of U/t and V/t , as shown in Fig. A.5. When U is moderately large and V is extremely large [$U/t \ll (V/t)^3$], $|J_1| \gg |K_3^\triangleright|, |K_3^\triangleleft|$ and hence $J_1^{\text{eff}} \sim J_1 \propto t^4/(V^2 U)$ is antiferromagnetic. Since $|J_2| \sim |K_4| \sim t^8/(V^4 U^3)$, the Hamiltonian effectively becomes an antiferromagnetic $J_1^{\text{eff}}\text{-}J_2$ Heisenberg model with four-spin ring exchange interaction K_4 . When J_2 is large enough, collinear antiferromagnetic order overcomes 120° order^{33,34}.

When U is extremely large and V is moderately large [$U/t \gg (V/t)^3$], $|K_3^\triangleright| \gg |J_1|, |K_3^\triangleleft|$ and hence $J_1^{\text{eff}} \sim K_3^\triangleright \propto -t^6/V^5$ is ferromagnetic. Since $|J_1| \gg |K_4| \gg |J_2|$, the

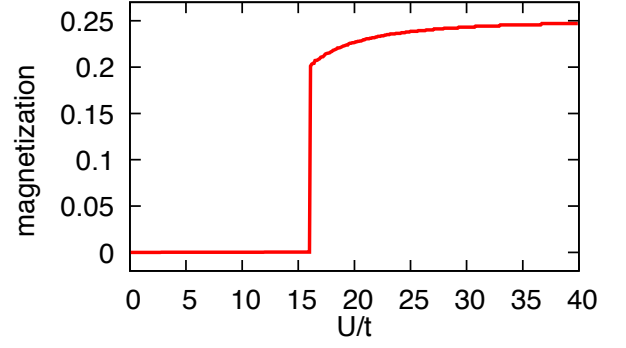


FIG. B.1: (Color online) Magnetization for the metallic state at $V = 0$ obtained by the Gutzwiller approximation for the $n = 3/2$ honeycomb lattice.

Hamiltonian effectively becomes a ferromagnetic Heisenberg model with small four-spin ring-exchange K_4 .

Finally, when $U/t \sim (V/t)^3$, t^6/V^5 terms in interactions $|J_1|$, $|K_3^\triangleright|$, and $|K_3^\triangleleft|$ nearly cancel out, and J_1^{eff} becomes extremely small $\sim t^8/V^7$. In this case, $J_2 \sim t^{12}/V^{11}$ is much smaller than J_1^{eff} , while $K_4 \sim t^8/V^7$ is comparable to J_1^{eff} . The Hamiltonian effectively becomes a four-spin ring-exchange model.

Appendix B: Gutzwiller approximation results on the extended Hubbard model on the honeycomb lattice at $n = 3/2$

In this appendix we present details on the calculations of the phase diagram for the extended Hubbard model on the honeycomb lattice at $n = 3/2$ by employing the Gutzwiller approximation.

B.1. In the absence of nearest-neighbor Coulomb interaction ($V = 0$)

We consider the case $U \neq 0$ and $V = 0$ on the doped honeycomb model at $3/4$ filling where charge order and/or ferromagnetism^{31,51} are expected to be stable.

As we have discussed in the main text, by using first the restricted Hartree-Fock method, we find the transition from a normal metal to a ferromagnetic metal at $U/t \sim 5$. When $U/t \gtrsim 6$, spins are fully polarized. An up-spin band becomes fully occupied, while a down-spin band becomes half occupied. Since the up- and down-spin bands are similar to the original honeycomb band, the Fermi level is located at the Dirac node of the down-spin band (semimetallic).

In order to assert the stability of the ferromagnetic state against quantum fluctuations beyond the mean-field treatment, we apply the Gutzwiller approximation. By assuming that the c and d orbitals are equivalent, we obtain the energy per bond as

$$\begin{aligned}
E(n_e, m, D) = & \frac{U}{3} 2D - t \langle T_{cd\uparrow} + T_{dc\uparrow} \rangle_0 \times \frac{(\sqrt{(1-2n_e+D)(n_e+m-D)} + \sqrt{(n_e-m-D)D})^2}{(n_e+m)(1-(n_e+m))} \\
& - t \langle T_{cd\downarrow} + T_{dc\downarrow} \rangle_0 \times \frac{(\sqrt{(1-2n_e+D)(n_e-m-D)} + \sqrt{(n_e+m-D)D})^2}{(n_e-m)(1-(n_e-m))},
\end{aligned} \tag{B1}$$

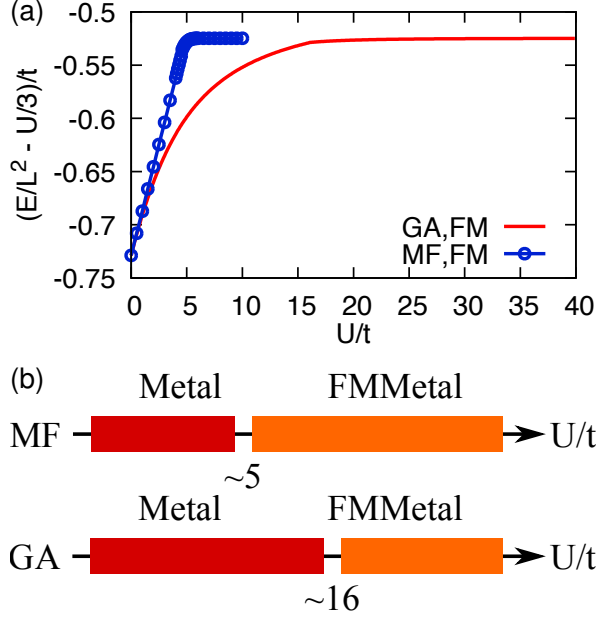


FIG. B.2: (Color online) (a) Comparison of the energies at $V = 0$ obtained for the honeycomb lattice at $3/4$ filling by Hartree-Fock and by the Gutzwiller approximation. The energy is saturated when the FM metal becomes fully polarized. (b) Schematic phase diagrams obtained by each method.

where $n_e = (n_{c,\uparrow} + n_{c,\downarrow})/2 = (n_{d,\uparrow} + n_{d,\downarrow})/2 = 3/4$ is the number of electrons, $m = (n_{c,\uparrow} - n_{c,\downarrow})/2 = (n_{d,\uparrow} - n_{d,\downarrow})/2$ is the magnetization, and $D = d_c = d_d$ is the number of doublons. Here, $\langle T_{cd\sigma} + T_{dc\sigma} \rangle_0$ is a function of $n_\sigma = n_e + \sigma m$. By numerically searching the energy minimum for $D \in [1/2, 9/16]$ and $m \in [0, |n_e - D|]$, we find a first-order transition from a normal metal to a ferromagnetic metal at $U/t \sim 16$, as shown in Fig. B.1. Inclusion of quantum fluctuations as done in the Gutzwiller approximation shifts the critical U to larger values than in the Hartree-Fock approximation (see Fig. B.2). Quantum fluctuations seem to favor a metallic state without ferromagnetism.

B.2. In the absence of on-site Coulomb interaction ($U = 0$)

We focus here on possible charge ordered states and phase separation for $U = 0$ and $V \neq 0$.

As we have discussed in the main text, the restricted

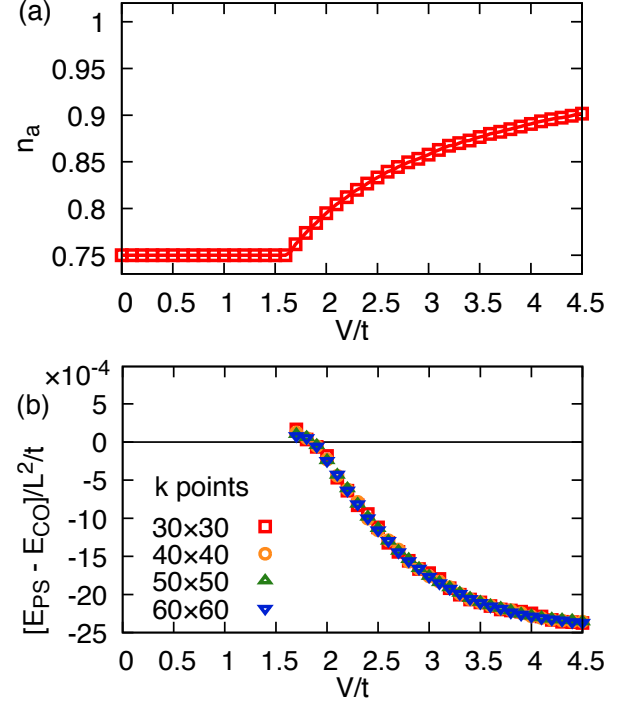


FIG. B.3: (Color online) Results for the honeycomb lattice at $3/4$ filling for $U = 0$ obtained by the Gutzwiller approximation. (a) Charge order parameter n_a as a function of V/t , from the uniform to the charge-ordered state. The number of electrons of charge-rich sites is given as $2n_a$. (b) Energy difference between charge ordered and phase separated states. They are nearly degenerate.

Hartree-Fock method finds the transition from a normal metal to a charge ordered metal at $V/t \sim 2$. Charge-poor sites form an emergent triangular structure as shown in Fig. 2 (c); however, we find it to be nonmagnetic.

We now proceed with the Gutzwiller approximation. Let us first focus on the uniform charge ordered state. We assume the absence of magnetization:

$$n_{c\uparrow} = n_{c\downarrow} = n_{c\sigma}, \tag{B2}$$

$$n_{d\uparrow} = n_{d\downarrow} = n_{d\sigma}. \tag{B3}$$

Since the total number of electrons is conserved ($n_{c\sigma} + n_{d\sigma} = 3/4$), the energy is given as a function of a single parameter $n_{c\sigma}$:

$$E(n_{c\sigma}) = 4Vn_{c\sigma} \left(\frac{3}{2} - n_{c\sigma} \right) - \frac{32}{3}t \langle T_{cd\sigma} + T_{dc\sigma} \rangle_0$$

$$\times \sqrt{n_{c\sigma}(1-n_{c\sigma}) \left(\frac{3}{2} - n_{c\sigma}\right) \left(n_{c\sigma} - \frac{1}{2}\right)}. \quad (\text{B4})$$

The expectation value of the hopping $\langle T_{cd\sigma} + T_{dc\sigma} \rangle_0$ is a constant since $n_{c\uparrow} + n_{d\uparrow} = n_{c\downarrow} + n_{d\downarrow} = 3/4$ is a constant. Hereafter, we abbreviate $t \langle T_{cd\sigma} + T_{dc\sigma} \rangle_0 |_{n_{c\sigma} + n_{d\sigma} = 3/4} = t_0 \sim 0.36$. By minimizing the energy for $n_{c\sigma} \in [3/4, 1]$, we find a phase transition from a normal metal to a charge ordered metal at $V_c/t_0 = 40/9$. The charge order parameter for $V > V_c$ is given as

$$n_{c\sigma} = \frac{3}{4} + \frac{1}{2} \sqrt{\frac{5}{4} - \left[1 - \left(\frac{8t_0}{3V}\right)^2\right]^{-1/2}}. \quad (\text{B5})$$

In the metallic phase the energy is $E = (9/4)V - 2t_0$, while in the charge ordered phase the energy is $E = V\{1 + \sqrt{1 - [8t_0/(3V)]^2}\}$. Thanks to the kinetic energy gain, the latter energy is lower than that of the fully charge ordered (2121 \cdots) insulating state ($E = 2V$).

Next, we consider the possibility of phase separation consisting of charge ordered insulator and metal phases. We separate the system into two regions: in the region κ a fully charge ordered insulating state ($n_{c\sigma} = 1$ and $n_{d\sigma} = 0$) is realized, while in the region $(1 - \kappa)$ a metallic state (the average number of electrons is n_e) is realized. In the

former region, there is no kinetic energy gain ($\langle T_{cd\sigma} \rangle = 0$) and no intersite Coulomb energy loss ($E_V = 0$ since $n_{d\sigma} = 0$). One only has to consider energy in the latter region, which is given as

$$E(\kappa, n_e) = (1 - \kappa) [4Vn_e^2 - 2t \langle T_{cd\sigma} + T_{dc\sigma} \rangle_0]. \quad (\text{B6})$$

The conservation of charge yields

$$2\kappa + (2n_e + 2n_e)(1 - \kappa) = 3, \quad (\text{B7})$$

$$\kappa = 1 - \frac{1}{4n_e - 2}, \quad (\text{B8})$$

which simplifies the energy

$$E(n_e) = \frac{1}{2n_e - 1} [2Vn_e^2 - t \langle T_{cd\sigma} + T_{dc\sigma} \rangle_0]. \quad (\text{B9})$$

Here, $\langle T_{cd\sigma} + T_{dc\sigma} \rangle_0$ is a function of n_e . If the energy is minimized for $\kappa > 0$, phase separation takes place. By numerically searching the energy minimum for $n_e \in [3/4, 1]$ ($\kappa \in [0, 1/2]$), we find a phase separated state for $V > V_c$. The charge ordered and phase separated states are found to be nearly degenerate, as shown in Fig. B.3, with the energy of the phase separated state being slightly lower.

-
- ¹ M. Imada, A. Fujimori, and Y. Tokura, *Rev. Mod. Phys.* **70**, 1039 (1998).
 - ² G. Baskaran, *Supercond. Sci. Technol.* **29**, 124002 (2016).
 - ³ H. Watanabe and M. Ogata, *J. Phys. Soc. Jpn.* **74**, 2901 (2005).
 - ⁴ L.F. Tocchio, C. Gros, X.-F. Zhang, and S. Eggert, *Phys. Rev. Lett.* **113**, 246405 (2014).
 - ⁵ R. Kaneko, L.F. Tocchio, R. Valentí, F. Becca, and C. Gros, *Phys. Rev. B* **93**, 125127 (2016).
 - ⁶ S. Reja, R. Ray, J. van den Brink, and S. Kumar, *Phys. Rev. B* **91**, 140403(R) (2015).
 - ⁷ C. Hotta and N. Furukawa, *Phys. Rev. B* **74**, 193107 (2006).
 - ⁸ M. Miyazaki, C. Hotta, S. Miyahara, K. Matsuda, and N. Furukawa, *J. Phys. Soc. Jpn.* **78**, 014707 (2009).
 - ⁹ L. Cano-Cortes, A. Ralko, C. Fevrier, J. Merino, and S. Fratini, *Phys. Rev. B* **84**, 155115 (2011).
 - ¹⁰ J. Merino, A. Ralko, and S. Fratini, *Phys. Rev. Lett.* **111**, 126403 (2013).
 - ¹¹ Y. Akagi and Y. Motome, *Phys. Rev. B* **91**, 155132 (2015).
 - ¹² J. Wen, A. Ruegg, C.-C. J. Wang, and G. A. Fiete, *Phys. Rev. B* **82**, 075125 (2010).
 - ¹³ K. Ferhat and A. Ralko, *Phys. Rev. B* **89**, 155141 (2014).
 - ¹⁴ F. Pollmann, K. Roychowdhury, C. Hotta, and K. Penc, *Phys. Rev. B* **90**, 035118 (2014).
 - ¹⁵ K. Roychowdhury, S. Bhattacharjee, and F. Pollmann, *Phys. Rev. B* **92**, 075141 (2015).
 - ¹⁶ E. Wawrzyńska, R. Coldea, E. M. Wheeler, I. I. Mazin, M. D. Johannes, T. Sörgel, M. Jansen, R. M. Ibberson, and P. G. Radaelli, *Phys. Rev. Lett.* **99**, 157204 (2007).
 - ¹⁷ E. Wawrzyńska, R. Coldea, E. M. Wheeler, T. Sörgel, M. Jansen, R. M. Ibberson, P. G. Radaelli, and M. M. Koza, *Phys. Rev. B* **77**, 094439 (2008).
 - ¹⁸ P. Fulde, A. N. Yaresko, A. A. Zvyagin, and Y. Grin, *Europhys. Lett.* **54**, 779 (2001).
 - ¹⁹ P. Fulde, K. Penc, and N. Shannon, *Ann. Phys.* **11**, 892 (2002).
 - ²⁰ S. Hayami, T. Misawa, Y. Motome, *JPS Conf. Proc.* **3**, 016016 (2014).
 - ²¹ Z. Y. Meng, T. C. Lang, S. Wessel, F. F. Assaad, and A. Muramatsu, *Nature* **464**, 847 (2010).
 - ²² S. Sorella, Y. Otsuka, and S. Yunoki, *Sci. Rep.* **2**, 992 (2012).
 - ²³ S. Raghu, X.-L. Qi, C. Honerkamp, and S.-C. Zhang, *Phys. Rev. Lett.* **100**, 156401 (2008).
 - ²⁴ C. Weeks and M. Franz, *Phys. Rev. B* **81**, 085105 (2010).
 - ²⁵ S. Capponi and A. M. Läuchli, *Phys. Rev. B* **92**, 085146 (2015).
 - ²⁶ J. Motruk, A.G. Grushin, F. de Juan, and F. Pollmann, *Phys. Rev. B* **92**, 085147 (2015).
 - ²⁷ D.D. Scherer, M.M. Scherer, and C. Honerkamp, *Phys. Rev. B* **92**, 155137 (2015).
 - ²⁸ M. Kurita, Y. Yamaji, M. Imada, *Phys. Rev. B* **94**, 125131 (2016).
 - ²⁹ E.V. Castro, A.G. Grushin, B. Valenzuela, M.A.H. Vozmediano, A. Cortijo, and F. de Juan, *Phys. Rev. Lett.* **107**, 106402 (2011).
 - ³⁰ A.G. Grushin, E.V. Castro, A. Cortijo, F. de Juan, M.A.H. Vozmediano, and B. Valenzuela, *Phys. Rev. B* **87**, 085136 (2013).
 - ³¹ T. Hanisch, G.S. Uhrig, and E. Müller-Hartmann, *Phys. Rev. B* **56**, 13960 (1997).

- ³² K. Pasrija and S. Kumar, Phys. Rev. B **93**, 195110 (2016).
- ³³ Th. Jolicoeur, E. Dagotto, E. Gagliano, and S. Bacci, Phys. Rev. B **42**, 4800(R) (1990).
- ³⁴ A. V. Chubukov and Th. Jolicoeur, Phys. Rev. B **46**, 11137 (1992).
- ³⁵ M. Roger, J.H. Hetherington, and J.M. Delrieu, Rev. Mod. Phys. **55**, **1** (1983).
- ³⁶ O.I. Motrunich, Phys. Rev. B **72**, 045105 (2005).
- ³⁷ T. Grover, N. Trivedi, T. Senthil, and P. A. Lee, Phys. Rev. B **81**, 245121 (2010).
- ³⁸ M. Holt, B.J. Powell, and J. Merino, Phys. Rev. B **89**, 174415 (2014).
- ³⁹ S.E. Korshunov, Phys. Rev. B **47**, 6165(R) (1993).
- ⁴⁰ K. Kubo, T. Momoi, Z. Phys. **B** 103, 485 (1997).
- ⁴¹ F. Becca, M. Capone, and S. Sorella, Phys. Rev. B **62**, 12700 (2000).
- ⁴² P.W. Anderson, G. Baskaran, Z. Zou, J. Wheatley, T. Hsu, B.S. Shastry, B. Doucot, S. Liang, Physica C **153**, 527 (1988).
- ⁴³ L. Balents, Nature **464**, 199 (2010).
- ⁴⁴ D. Poilblanc and H. Tsunetsugu, *Mobile Holes in Frustrated Quantum Magnets and Itinerant Fermions on Frustrated Geometries*, Springer Series in Solid-State Sciences, edited by Claudine Lacroix, Philippe Mendels, and Fred-eric Mila, Vol. 164 (Springer, Berlin, Heidelberg, 2011), p. 563.
- ⁴⁵ F. Mila and X. Zotos, Europhys. Lett. **24**, 133 (1993).
- ⁴⁶ K. Penc and F. Mila, Phys. Rev. B **49**, 9670 (1994).
- ⁴⁷ M. Vojta, A. Hübsch, and R.M. Noack, Phys. Rev. B **63**, 045105 (2001).
- ⁴⁸ L.F. Tocchio, F. Becca, and C. Gros, Phys. Rev. B **83**, 195138 (2011).
- ⁴⁹ Y. Iqbal, F. Becca, S. Sorella, and D. Poilblanc, Phys. Rev. B **87**, 060405(R) (2013).
- ⁵⁰ S. Depenbrock, I.P. McCulloch, and U. Schollwöck, Phys. Rev. Lett. **109**, 067201 (2012).
- ⁵¹ Y. Nagaoka, Phys. Rev. **147**, 392 (1966).
- ⁵² Y. Sugita and Y. Motome, J. Phys. Soc. Jpn. **85**, 073709 (2016).
- ⁵³ D. Tahara and M. Imada, J. Phys. Soc. Jpn. **77**, 114701 (2008).
- ⁵⁴ T. Ogawa, K. Kanda, and T. Matsubara, Prog. Theo. Phys. **53**, 614 (1975).
- ⁵⁵ F.C. Zhang, C. Gros, T. M. Rice, and H. Shiba, Supercond. Sci. Technol. **1** 36 (1988).
- ⁵⁶ C. Gros, Phys. Rev. B **38**, 931(R) (1988).
- ⁵⁷ M. Capello, F. Becca, M. Fabrizio, S. Sorella, and E. Tosatti, Phys. Rev. Lett. **94**, 026406 (2005).
- ⁵⁸ L.F. Tocchio, F. Becca, A. Parola, and S. Sorella, Phys. Rev. B **78**, 041101(R) (2008).
- ⁵⁹ S. Yunoki and S. Sorella, Phys. Rev. B **74**, 014408 (2006).
- ⁶⁰ R.H. McKenzie, J. Merino, J.B. Marston, and O.P. Sushkov, Phys. Rev. B **64**, 085109 (2001).